AMERICAN
METEOROLOGICAL
SOCIETY

Journal of Hydrometeorology

EARLY ONLINE RELEASE

This is a preliminary PDF of the author-produced manuscript that has been peer-reviewed and accepted for publication. Since it is being posted so soon after acceptance, it has not yet been copyedited, formatted, or processed by AMS Publications. This preliminary version of the manuscript may be downloaded, distributed, and cited, but please be aware that there will be visual differences and possibly some content differences between this version and the final published version.

The DOI for this manuscript is doi: 10.1175/JHM-D-17-0036.1

The final published version of this manuscript will replace the preliminary version at the above DOI once it is available.

If you would like to cite this EOR in a separate work, please use the following full citation:

Ralph, F., S. Iacobellis, P. Neiman, J. Cordeira, J. Spackman, D. Waliser, G. Wick, A. White, and C. Fairall, 2017: Dropsonde Observations of Total Integrated Water Vapor Transport within North Pacific Atmospheric Rivers. J. Hydrometeor. doi:10.1175/JHM-D-17-0036.1, in press.

© 2017 American Meteorological Society

Manuscript (non-LaTeX)
Click here to download Manuscript (non-LaTeX) AR Transport_Format4JHM_Revised.docx

AMERICAN METEOROLOGICAL SOCIETY 1919

Dropsonde Observations of Total Integrated Water Vapor Transport within North Pacific Atmospheric Rivers

F. M. Ralph[1], S. F. Iacobellis[1],
P. J. Neiman[2],
J. M. Cordeira[3],
J. R. Spackman[2,4],
D. E. Waliser[5],
G. A. Wick[2], A.B. White[2], and C. Fairall[2]

[1]UC San Diego, Scripps Institution of Oceanography, Center for Western Weather and Water Extremes, La Jolla, CA
[2]NOAA/OAR/ESRL/Physical Sciences Division, Boulder, CO
[3]Plymouth State University, Plymouth NH
[4]Science and Technology Corporation, Washington, DC
[5]NASA/Jet Propulsion Laboratory, Pasadena, CA

Revised: 1 July 2017 (for submission to J. Hydrometeor.)

Corresponding Author:
Sam F. Iacobellis
9500 Gilman Drive, Dept 0224
La Jolla, CA 92093-0224
siacobellis@ucsd.edu

PRELIMINARY ACCEPTED VERSION

Abstract

Aircraft dropsonde observations provide the most comprehensive measurements to date of horizontal water vapor transport in atmospheric rivers (AR). The CalWater experiment recently more than tripled the number of ARs probed with the required measurements. This study uses vertical profiles of water vapor, wind, and pressure obtained from 304 dropsondes across 21 ARs. On average, total *water vapor* transport (TIVT) in an AR was $4.7\times10^8 \pm 2\times10^8$ kg s^{-1}. This magnitude is 2.6 times larger than the average discharge of *liquid water* from the Amazon River. The mean AR width was 890 ± 270 km. Subtropical ARs contained larger IWV but weaker winds than midlatitude ARs, although average TIVTs were nearly the same. Mean TIVTs calculated by defining the lateral "edges" of ARs using an IVT-threshold versus an IWV-threshold produced results that differed by less than 10% across all cases, but did vary between midlatitudes and subtropical regions.

1. Introduction

The global atmospheric water budget is a subject of ongoing research. Recent evaluations of global climate model representations of precipitation, evaporation, and moisture transport compared to observed river discharges into oceans (*Trenberth et al.* 2011) concluded: "Their differences reveal outstanding issues with atmospheric models and their biases …" One reason for their differences is that horizontal water vapor transport in climate models is sensitive to grid size (e.g., *Hughes et al.* 2012; *Demory et al.* 2014). Demory notes "... as [model] resolution is increased, precipitation decreases over the ocean and increases over the land. This is associated with an increase in atmospheric moisture transport from ocean to land, which changes the partitioning of moisture fluxes that contribute to precipitation over land from less local to more non-local moisture sources." This reasoning raises the question of what amount of water vapor transport is correct, and thus how well atmospheric rivers (AR) are represented, since they are responsible for 90% or more of horizontal water vapor transport in midlatitudes (e.g., *Zhu and Newell* 1998; *Ralph et al.* 2004). To help address this challenge, the data and analyses presented herein use field observations from research aircraft during the recent CalWater field experiments (*Ralph et al.* 2016), and from earlier experiments. The CalWater data more than triple the number of suitably observed cases available.

The crucial role of ARs in determining the water vapor and precipitation distribution and variability in and near the midlatitudes makes them a key player in the water cycle. These relatively narrow (<1000 km), low-altitude (75% of water transport within lowest 2.5 km), elongated (>~2000 km) corridors of strong horizontal water vapor transport occur over most mid-latitude areas of the globe (*Waliser et al.* 2012b). Their impacts are becoming increasingly recognized, particularly for the western, and even central, U.S. as well as other areas in the world where they are implicated in extreme precipitation and most major flooding events on the west coasts of mid-latitude continents (*Ralph et al.* 2006, 2011; *Neiman et al.* 2008a, b, 2011; *Leung and Qian* 2009; *Guan et al.* 2010, 2013; *Dettinger et al.* 2011; *Lavers et al.* 2011, 2012; *Moore et al.* 2012; *Kim et al.* 2013; *Viale and Nunez* 2011). For example, *Ralph et al.* (2006) showed that the seven largest mean daily flow events during 1997-2006 period on northern California's Russian River are directly attributed to heavy precipitation during landfalling ARs. Similarly, *Neiman et al.* (2011) showed most annual peak streamflow events in Washington were associated with ARs. Studies in Europe (*Stohl et al.* 2008; *Lavers et al.* 2011, 2012) and South America (*Viale and Nunez,* 2011) have come to similar conclusions. In conjunction with these flooding hazards, ARs also make vital contributions to regional water supply and can be key in breaking droughts. For example, 25–50% of the water supply (i.e., snow pack and rain) in the U.S. west coast states is delivered by only a few AR events (*Guan et al.* 2010; *Dettinger et al.* 2011; *Ralph et al.* 2013), and roughly 40% of drought breaks in California were associated with a period of landfalling ARs (*Dettinger* 2013). Additionally, recent diagnoses of new climate projections of annual precipitation in California have found that the largest contributor to intermodel variability in this key parameter is caused by how the strongest precipitation events (i.e., in this area – ARs) are represented (*Pierce et al.* 2013).

Most earlier AR studies have depended upon satellite-observed vertically integrated water vapor (IWV) using SSM/I satellite data (e.g., *Ralph et al.,* 2004; *Wick et al.,* 2013), or on reanalyses and model-derived analyses (e.g., *Neiman et al.,* 2008; *Lavers et al.,* 2011; *Cordeira et al.,* 2013). Although the IWV measurements provide a useful proxy for AR water vapor transport, anecdotal evidence suggests there are numerous instances when the IWV measurements identify an AR in the presence of very little horizontal water vapor transport occurring (often in the “equatorward tail” of an IWV AR signature).

In spite of their importance, very few measurements have been available to observationally quantify and validate the amount of water vapor *transported* in ARs. These validations have focused on case studies in which dropsondes released from research aircraft across an AR are used to determine the horizontal water vapor transport (*Ralph et al.,* 2004, 2011; *Neiman et al.,* 2014a). The dropsondes measure wind, water vapor, temperature and pressure as they descend. One of the goals of the “CalWater” program of field studies (*Ralph et al.,* 2016) has been to collect a much larger set of such observations so as to better quantify and understand ARs over the Pacific Ocean. This paper presents analyses combining the earlier flight data with the new CalWater measurements. Additionally, these data allow for quantitative comparison of the well-established IWV-based threshold (20 mm) used to define the lateral “edges” of an AR with the emerging use of an integrated vapor transport (IVT) threshold [typically 250 kg m^{-1} s^{-1}; e.g., *Moore et al.* (2012); *Rutz et al.* (2014), though *Mahoney et al.* (2016) uses 500 kg m^{-1} s^{-1} for the southeast U.S. - a region with greater background water vapor, and a variable IVT threshold was used by *Lavers et al.* (2012) and *Guan et al.* (2015)].

In February 2014, the NOAA G-IV research aircraft sampled 10 ARs over the northeast Pacific Ocean as part of an "early-start" deployment for the CalWater2 project. On five of these flights, multiple dropsondes were deployed in a line crossing the AR to sample the total AR water vapor transport (AR transport). During the main deployment of CalWater2, the NOAA G-IV aircraft sampled transects across another seven ARs in early 2015 while the USAF C-130 sampled four ARs in early 2016. These recent data more than quadrupled the overall number of such cross-AR airborne samples suitable for calculating AR water vapor transport. The sampling also allowed for analysis to explore what number of dropsonde samples are needed to accurately quantify the full water vapor transport of an AR through a cross section across an AR. The "AR transport" is defined here as the total IVT (TIVT), and is calculated as the horizontal integral of IVT across the AR transect perpendicular to the direction of mean vapor transport. Analysis of these 12 new samples, in combination with the five previous samples from the preceding 10 years, from a Hawaii-based experiment in 2005 (*Ralph et al.*, 2011) and Winter Storms and Pacific Atmospheric Rivers (WISPAR) in 2011 (*Neiman et al.,* 2014a), are used here to comprehensively investigate the observed amount of water vapor transport in ARs, and to compare IWV-based and IVT-based AR detection criteria.

2. Data

Vertical profiles of dropsonde measurements gathered from 37 research flights that observed ARs over the Northeast Pacific Ocean during the 1998-2016 period were examined (Table 1). In order to be considered in the present analysis, each profile was required to have no vertical data gaps exceeding 50 hPa within the surface-to-500-hPa layer. Applying this criterion yielded a total of 1052 profiles of dropsonde measurements, with the number of dropsondes per flight varying from 4 to 59. The IWV and IVT were calculated from each profile using:

$$\mathrm{IWV} = \frac{1}{g}\int_{p_{sfc}}^{p_{top}} q \, dp$$

and

$$\mathrm{IVT} = \frac{1}{g}\int_{p_{sfc}}^{p_{top}} q\boldsymbol{V} \, dp$$

where g is gravity, q is the specific humidity, V is the wind velocity, and p_{top} is the upper limit of data from each dropsonde. The value of p_{top} varies among the dropsondes, thus impacting comparison of calculated values of IWV and IVT. We assume this impact is not significant since we required dropsondes to provide data throughout the surface-to-500-hPa layer that contains the vast majority of atmospheric water vapor (e.g., only 3% of the total atmospheric water vapor and 5% of the total IVT was contained in the 500-200-hPa layer based on 400 dropsondes with data extending above 200 hPa). The AR water vapor transport is calculated from transects that meet the following three criteria:

- transect had to consist of at least 9 dropsondes (to help insure adequate observational coverage of the AR core; see section 3e assessment of sensitivity of TIVT to dropsonde spacing);
- IWV > 20 mm or |IVT| > 250 kg m^{-1} s^{-1} at a minimum of three interior dropsonde locations;
- IWV < 20 mm or |IVT| < 250 kg m^{-1} s^{-1} at both ends of the transect

The threshold value of IWV=20 mm is motivated by *Ralph et al.* (2004) and *Neiman et al.* (2008a), whereas the threshold value of |IVT|=250 kg m^{-1} s^{-1} is motivated by *Moore et al.* (2012) and *Rutz et al.* (2014).

Application of these conditions to the dropsonde data from the 37 flights in Table 2 yielded 21 individual transects (total of 304 dropsondes) deemed to contain enough observations to adequately sample an AR cross-section. However, in some of these 21 cases the dropsonde transect did not extend far enough away from the center on one side (usually the equatorward side) to completely sample the AR using the above IWV and IVT criteria. In other words, the first or last dropsonde in the transect was still within the AR using the IWV>20mm and

IVT>250 kg m^{-1} s^{-1} thresholds. To increase the number of available study cases, the criteria was subjectively relaxed. This resulted in 4 sub-categories of cases:

A) AR defined using stated IWV and IVT thresholds (7 cases).

B) Lateral edges defined if first or last dropsonde reported IWV and/or IVT within 15% of respective threshold (6 cases).

C) Lateral edge of equatorward side of AR defined using IVT threshold but not IWV threshold (4 cases). All of these were subtropical cases where the equatorward boundary of the AR was within a large region of high IWV based on Special Sensor Microwave Imager (SSMI) IWV imagery. This suggests that the main advective dynamics associated with the AR was completely sampled by the dropsondes and also illustrates a drawback to using the IWV threshold in these sub-tropical regions.

D) A lateral edge of AR not defined using IVT threshold but numerical model analyses indicates that lateral edge of AR was within 200 km of end of dropsonde transect. (4 cases). For these cases, calculations of TIVT and AR width using Global Forecast System (GFS) 0.5° analysis products (EMC, 2003) were performed along i) the partial transect defined by the available dropsondes; and ii) the full transect with the missing AR edge defined from GFS IVT values using the analysis time closest to the time at mid-transect. Comparison of calculations (i) and (ii) indicate that using the partial transect defined by the available dropsondes results in underestimates of 8% in TIVT and 16% in AR width.

Separate calculations of TIVT (as well as other variables) are made for each of the thresholds used to determine AR boundaries: (1) IWV>20 mm or (2) IVT>250 kg m^{-1} s^{-1} for transects that occur in the subtropics (central latitude < 33°N) and midlatitudes (central latitude >33°N).

The large-scale spatial distribution of SSMI-derived IWV (*Wentz et al*, 2012) at the time of each transect are shown in Figures 1 and 2, whereas the transect values of IWV and IVT magnitude are shown in Figure 3. Examination of many of the SSMI-derived IWV analyses illustrate a well-defined corridor of enhanced IWV that is a common signature of an AR (e.g., *Ralph et al.*, 2004; *Neiman et al.*, 2008), whereas examination of the transect values of IVT magnitude reveals that each transect contains IVT magnitudes > 250 kg m^{-1} s^{-1}. Transects are mostly found over the Eastern North Pacific between 17°N to 49°N in a location that frequently experiences AR conditions during winter months (Figure 4).

3. Analysis

a. Overall mean and comparison of IWV- and IVT-based methods

The 21-case mean TIVT is 4.7×10^8 kg s^{-1}, using the IVT magnitude threshold of 250 kg m^{-1} s^{-1}; the IWV threshold of 2 cm yielded an average TIVT that was 8% smaller. The average AR width is 886 km using the IVT magnitude threshold, which is just 2% larger than that derived using the IWV threshold (note that the width is greater than that of Ralph et al. 2004 because that study limited cases to those <1000 km wide, and did not address subtropical cases as much; as shown in Table 2, the subtropical cases are much broader than are the midlatitude cases – 1144 km vs 647 km). The small differences obtained using the two thresholding methods indicate that the IVT magnitude threshold of 250 kg m^{-1} s^{-1} corresponds well to the well-established IWV threshold of 2 cm. The IVT magnitude threshold method has some distinct advantages when the AR transects are subdivided by latitude. First, the IVT magnitude threshold is less sensitive to varying background IWV conditions as evidenced by the 77% greater average width of ARs in the subtropics as compared to ARs in the midlatitudes using the IWV threshold and a 5% reduced average width of ARs in the subtropics as compared to ARs in the midlatitudes using the IVT magnitude threshold. Second, the IVT magnitude threshold produces results that are far more consistent between subtropical and midlatitude conditions (i.e., the average TIVT and AR widths differ between the regions by 1% and 5% respectively for the IVT method, compared to 24% and 77% using the IWV method). Third, orographic precipitation, which is an important driver for both total annual precipitation and individual extreme precipitation events on many west coasts of continents, is driven much more by the flux of water vapor up a mountain slope (i.e., the upslope component of IVT) than by simply the amount of water vapor (IWV).

b. Comparison of all individual AR transects

The 21 individual transects, shown in Figure 3, represent a extensive range of ARs as measured by the characteristics listed in Table 2 and by their structures in IWV seen in Figures 1 and 2. In some cases the IWV criteria was not met, but IVT was (e.g., AR 4), while in others the IWV criteria was met, but the IVT criterion was only barely met (e.g., AR 10). Generally, the subtropical ARs did not have a well-defined southern (warm) edge based on IWV criteria, but did for IVT criterion. AR 3 had a broad region of large IWV but very weak IVT on its cold side, and the case with the strongest IVT (AR 7) had only slightly greater max IWV than other ARs. Conversely, an IVT magnitude transect with relatively small values (AR 10) has IWV values that are larger than many other transects over much of its width. These differences highlight the importance of the horizontal wind field, and how IVT provides a more robust criterion for identifying ARs. The analysis hereafter focuses on the application of IVT magnitude threshold method.

c. Composite AR characteristics

To best synthesize the information from the many AR observations, the data from all 21 transects are averaged into one composite transect. Thus, this transect represents the mean characteristics of the width and TIVT of all the cases observed. To provide the synoptic context, a composite of the plan view perspective is also shown. The resulting composite analysis (methodology described below) based on all 21 ARs is provided in Figures 5 and 6. Separate composite analyses for subtropical and midlatitudes cases are shown in Figures 7-10.

Plan view composites [Figures 5, 7, and 9] were produced using Climate Forecast System (CFS) products (reanalysis for 2005 and 2011 ARs and operational analyses for 2014-2016 ARs) at 0.5 degree resolution. IWV and IVT were computed from 1000 hPa to 250 hPa for each AR listed in Table 2. Composites were formed by referencing (without rotation) the horizontal IWV, IVT and surface pressure fields to the latitude and longitude of the IVT maximum for each AR.

Cross-sectional view composites [Figures 6, 8, and 10] were produced using dropsonde measurements for each AR. For the vertical cross-section view, IVT was calculated as a function of pressure and horizontal distance along each AR transect and then normalized to match the mean width and mean TIVT of all ARs considered. The along-transect vertically integrated IVT and IWV from each AR was normalized to the AR width.

On average, an AR is associated with an extratropical cyclone and is located ~1000 km southeast of the parent low pressure center (Figure 5). The regions of composite IVT magnitudes > 250 kg m^{-1} s^{-1} and precipitation rates > 2 mm 6-hr^{-1} extend ~2500 km from southwest to northeast and is embedded within a 3500 km-long region of IWV > 2 cm oriented from southwest to northeast (these lengths are shortened by the compositing method, because it does not rotate the original reanalysis fields from each case). The composite maximum IVT magnitude is ~500 kg m^{-1} s^{-1}, the maximum IWV is >3 cm, and maximum precipitation rate 8 – 10 mm 6-hr^{-1}. The composite IWV pattern looks remarkably similar to a typical SSM/I satellite image. The composite vertical cross section (Figure 6 top panel) shows the vertically sloping character (upward toward the cold side) of the core of the horizontal water vapor flux above ~900 hPa. The baroclinicity of the region is indicated by the slope of the freezing level, which descends more than 1 km on average across the AR, and by the presence of an upper-level jet stream wind maximum >45 m s^{-1}. Most (75%) of the IVT (i.e., H75) is found below about 2.9 km MSL and the region of the upper-level jet stream wind above 8 km contains just 5% of the IVT. The rather symmetric distribution of IVT across the AR is evident in bottom panel of Figure 6. The close correspondence of the IWV-based (2 cm) and IVT-based threshold (250 kg/m/s) on the northwest (cold) edge of the AR is seen in this figure, as is the lack of correspondence at the southeastern (warm) edge.

Table 2, Figure 3, and Figures 7-10 reveal some important differences between subtropical and midlatitude ARs. In particular, note that the maximum IWV values in the subtropical cases averaged 41% more than the midlatitudes cases (41.3 vs 29.3 mm), likely due to the general equatorward increase in IWV. In contrast, the average maximum IVT, the average TIVT, and the average width in the midlatitudes all varied by less than 5% from the average values in the subtropics (using IVT threshold method). This difference results largely from the fact that winds are often much stronger in the midlatitude events (mean maximum 925 hPa wind speed was 30.2 m s^{-1} in midlatitude transects vs 22.0 m sec^{-1} in subtropical transects), although the average direction of the full-layer mean transport is nearly identical (226° vs 228°), i.e., transporting water vapor from the southwest to northeast. The precipitation distributions also differ, with the midlatitude composite showing structure characteristic of a comma cloud typically found with extra tropical cyclones, while the subtropical cases show somewhat less organized precipitation structure and the maximum larger composite rain rates are greater than the midlatitude composite. In both cases the maximum precipitation is northeast of the center of the cross section.

Differences in the vertical structure between subtropical and midlatitudes ARs is also revealed by this analysis. The upper-level (ULJ) and low-level jets (LLJ) are both stronger in the midlatitudes ARs, with the ULJ and LLJ averaging just over 50 m s^{-1} and 25 m s^{-1} in the midlatitudes, and 40 m s^{-1} and 15 m s^{-1} in the subtropics. Baroclinicity is evident in both sections (based on slope in the freezing level), but is greater in mid-latitudes. The atmosphere is generally cooler in the midlatitude cases with the 0°C level averaging 3.3 km and 1.8 km MSL on the south and north edges of the midlatitudes ARs, versus 4.2 and 3 km MSL for the subtropical ARs. Intriguingly, the AR core (as defined by either the largest IVT in the traces shown in bottom panels, or by the largest low-level vapor transport in the cross sections in top panels of Figures 6, 8, and 10) is closer to the southern edge of the AR in the midlatitudes cases than the subtropical ones, and the horizontal vapor transport in the AR core (as defined by the low-level vapor transport) is roughly 10% greater in the midlatitudes cases. Both exhibit a slope poleward with height in terms of the location of maximum transport within the AR. Remarkably, the altitude beneath which 75% and 99% of IVT occurs is nearly identical for the midlatitudes and subtropical ARs.

d. Toward a scaling of AR water vapor transport

Given the vital role of ARs in both global water vapor transport and in creating extreme precipitation, there is potential value to both predictive and diagnostic studies in identifying, tracking and communicating the relative magnitude of an AR event in terms of bulk water vapor transport. However, the units are rather hard to grasp without context. The development of a simple scale for AR strength can overcome this. This simple scale would be analogous to the existence of a "flood stage" for terrestrial streamflow, and of the use of the "Sverdrup" for ocean current transport (1 "Sverdrup" = 10^6 m^3 s^{-1} of ocean current transport). The most analogous variable for ARs is TIVT, which ranges from 1.33 to 8.33 x10^8 kg s^{-1} in the cases sampled here. Although this paper triples the number of such measurable cases available, it is clear that more extreme events exist but have not been observed. For convenience and simplicity, it could be useful to consider ranking ARs by their intensity in terms of multiples of 10^8 kg s^{-1}. Future work will identify the frequency of occurrence of AR intensities.

Experience suggests that maximum IVT (IVT_{MAX}) is another useful parameter that can help assess the strength of an AR. Although it represents a single "point" in space and time, rather than a flux of an entire AR, the values are easily displayed on traditional weather maps. A comparison of IVT_{MAX} with TIVT for the 21 cases shows a 83% correlation while IWV_{MAX} vs TIVT has a correlation of only 20% (Figure 11). A comparison of IWV and IVT from all AR dropsondes (not shown) showed that increasing values of IVT are somewhat associated with increasing values of IWV, however the correlation between the two parameters is relatively low at 0.53. Based on these results, the use of IWV as a proxy for IVT is not recommended.

e. Dropsonde Horizontal Resolution

The data from several well sampled cases are used to assess the sensitivity of AR transport (TIVT) to dropsonde horizontal spacing and vertical resolution. This sensitivity analysis is of practical importance for future field campaigns examining ARs, due to the relatively high cost of the dropsondes.

In this sensitivity experiment, a series of sequential calculations of $TIVT_i$ (i=1-N) are made across an AR. The first calculation, $TIVT_1$ utilizes all available dropsondes and serves as the control. Subsequent calculations remove interior dropsondes so that the average distance between dropsondes doubles. Thus the horizontal spacing would increase relative to the control case by a factor of 2 for $TIVT_2$, a factor of 4 for $TIVT_3$, a factor of 8 for $TIVT_4$, and so on (dropsondes on each end of the transect are the same throughout to insure the width of the AR did not change).

For this experiment TIVT was calculated using the IVT>250 kg m^{-1} s^{-1} threshold. Only AR events 1, 4, 5, 6, 8, and 9 were used in this experiment because they had i) a relatively uniform dropsonde spacing (S) across the AR $(\sigma_S/\langle S\rangle < 0.40)$, where σ_s is the standard deviation of dropsonde spacing; and ii) at least 9 dropsondes across the AR allowing for an increased spacing of at least 4. The mean dropsonde spacing in each of these 6 AR events varied from 63 to 95 km with a mean of 80 km. Figure 12 shows how the sequential removal of specific dropsondes was performed to increase dropsonde spacing by a factor of 2X, 4X, and 8X using AR event 9 as an example.

When the spacing between dropsondes was doubled, the absolute difference in TIVT varied from 1-9% with a mean value of 5% (see Figure 13). When the dropsonde spacing was increased by a factor of 4, the absolute TIVT difference from the control case ranged from 4-18%, although it should be noted that results from 5 of the cases varied from 4-10% with a single case at 18%. The two experiments with enough dropsondes across the AR to allow an increase in spacing by a factor of 8 had a mean absolute difference of 28%.

A parallel experiment was carried using the 0.5° GFS analysis data described earlier. In this experiment, GFS analysis data was linearly interpolated to each dropsonde location and then the procedure was carried out as before, that is increasing the spacing between dropsonde sites by factors of 2, 4, and 8 and calculating the TIVT. Only 3 (events 6, 8, and 9) of the 6 cases were examined in this parallel experiment due to limited availability of 0.5° GFS analysis products.

The absolute differences in TIVT due to increasing spacing using the interpolated GFS analysis products was about 1/3 of the differences calculated when using the dropsonde values. The smaller differences are likely due (at least in part) to i) the interpolation of the GFS products to the dropsonde locations which would have a smoothing effect on horizontal variations; and ii) numerical weather model products having (in general) smoother varying horizontal fields than the real atmosphere.

The results of this sensitivity experiment illustrate how the accuracy of the calculated TIVT across an AR degrades as the dropsonde resolution increases and may provide at least a first order estimate for cost analyses during the planning of future research flights. Based on these results, it is recommended that future airborne AR experiments focused on TIVT normally use a dropsonde spacing of 100 km, which will not seriously degrade TIVT measurements and would on average still provide 8 samples within AR conditions. Other AR science or objectives (e.g., numerical weather prediction and data assimilation) may require closer spacing.

f. Comparison to GFS analysis products

Dropsonde derived values of IWV, IVT and TIVT along transects from 14 AR cases were compared to values from GFS analysis products (0.5° grid) to provide an initial estimate on how well numerical models simulate these important quantities. Admittedly, the GFS model is just one of many numerical models and the brief analysis provided here is simply a starting point for a more comprehensive analysis involving multiple models.

Values of IWV and IVT were calculated using the GFS humidity and wind fields at each dropsonde location in the transects using linear interpolation and model analysis time closest to the time at mid-transect.

Figure 14 shows the difference (GFS-dropsondes) in IWV and IVT along 14 of the 21 AR transects shown in Table 1 (GFS products at 0.5° resolution were not available for cases 1-5, 7 and 10). In general, the GFS model overestimates both IWV and IVT in the subtropical cases and to a lesser extent in the mid-latitude cases. There is a consistent trend for the GFS to overestimate IVT on the poleward side of subtropical ARs and on the southern side of mid-latitude ARs.

Comparisons of TIVT calculated from the dropsondes and GFS model are found in Figure 15. Values of TIVT calculated over the entire column (1000-300 hPa) (FIgure 15a) show a relatively close correspondence between dropsondes and the GFS model with the GFS model slightly overestimating TIVT (with the exception of a single outlier case) which is consistent with the results shown in Figure 14.

Values of TIVT along each transect were calculated in 50 hPa layers to examine the vertical structure. The vertical profiles of this layer-TIVT are shown in Figure 15b where the values are normalized by their respective TIVT calculated over entire atmospheric column. The difference between the layer-TIVT vertical profiles shown in Figure 15c indicate that the mean differences are up to about 2% of the total atmospheric column TIVT at any given height. However, there is a consistent trend for the GFS model to overestimate the TIVT contribution below about 925 hPa and above 550 hPa and to underestimate the TIVT contribution in between these pressure levels.

4. Discussion

Measurements from 21 AR events described above provides the best observations to date of the intensity, size and structure of a relatively large number of ARs. This structure is summarized schematically in Figure 16. Mean characteristics are shown based on using the IVT threshold of 250 kg m^{-1} s^{-1} to define the lateral boundary. The schematic highlights a type of dipole structure in the vertical (Figure 16b). The upper portion is the well-known upper-level jet, which is where the strongest winds are found, but where water vapor transport is minimal due the extreme cold, and thus dryness of the air. The lower portion represents the atmospheric river, which carries the vast majority of the horizontal water vapor transport, even though the winds are not as strong as in the upper-level jet.

For each transect the total horizontal transport of water vapor within the domain of the AR was observed. It is analogous to a measurement of streamflow in a terrestrial river, which is measured in m^3 s^{-1}. However, the flux in an AR is in the form of water vapor rather than liquid, the edges are less well defined, and TIVT is measured in kg s^{-1}. Another analogy is in terms of ocean currents and their transport of ocean water. Like ARs, they exist without solid lateral boundaries, and nonetheless measurements of their transport has been of great utility in ocean science.

Mean flow rate (i.e., TIVT) within the 21 observed ARs in Table 2 was about 4.7x10^8 kg s^{-1} with a maximum value of about 8.3x10^8 kg s^{-1}. The width varied from 400-1400 km with a mean of 890 km (values based on IVT threshold). The average meridional water vapor flux in these 21 ARs was 3.1x10^8 kg s^{-1}, or approximately 25% of the global average across 35°N as reported in *Zhu and Newell* (1998), thus suggesting that the mean of these 21 cases is representative of a global mean. The total instantaneous water vapor flux in an average AR is roughly equivalent to the flux of liquid water into the Gulf of Mexico from 27 Mississippi Rivers, or to the discharge of 2.6 Amazon Rivers (*Kammerer*, 1990) (see Table 3). For comparison, the total discharge of fresh water into the oceans is roughly 10^6 m^3 s^{-1} (*Dai et al* 2009, *Seo et al* 2012).

The results show that the relative importance of the wind field in producing an AR increases with latitude. At more subtropical latitudes, an AR may exist primarily due to very high concentrations of water vapor, with relatively weak winds. As latitude increases towards the pole it becomes increasingly necessary to have both strong winds and adequate water vapor. In general, the AR width and TIVT are less dependent on latitude when IVT is used to define ARs than when IWV is used. Thus, IVT represents a more robust threshold across a wider range of conditions than does IWV.

The measurement of water transport rates in ocean currents has been routinely performed over many decades using vertical arrays of current meters. However, the more spatial and temporally transitory nature of ARs currently limits our observational methods over oceans to aircraft-deployed dropsondes, and over land to radiosondes and AR observatories (AROs; *White et al.*, 2013). AROs include wind profiling radars and GPS-met IWV sensors that can monitor AR “bulk water vapor flux”, which is a proxy for IVT (*Ralph et al.*, 2013). Seven AROs are now emplaced along the US West Coast and it is possible that more research aircraft missions will be conducted.

The emergence of the AR concept reflects an understanding that atmospheric horizontal water vapor transport in the midlatitudes and subtropics occurs almost entirely within relatively narrow “filaments.” There are typically 3-5 in existence in each hemisphere, each contributing roughly a quarter of the global water vapor transport in midlatitudes. Taken together, eight ARs globally transport an amount of water vapor equivalent to roughly four times the discharge of the world’s rivers.

It is envisioned that future work will use global reanalyses to evaluate the representativeness of the means derived from the airborne data presented here, and will include quantitative evaluation of weather and climate reanalyses, forecasts and climate projections through use of these unique observations. The increasing focus on the horizontal transport dimension of the atmospheric water vapor budget complements the long-standing and extensive exploration of vertical water vapor fluxes from the earth’s surface and deep convection.

Acknowledgments

This research was supported by funding provided by Awards NA13OAR4830231 and NA13OAR4830271 from the National Oceanographic and Atmospheric Administration (NOAA). SSM/I data are produced by Remote Sensing Systems and data available at www.remss.com/missings/ssmi. GFS analysis products were downloaded from http://emc.ncep.noaa.gov. DEW's contribution to this study was carried out on behalf of the Jet Propulsion Laboratory, California Institute of Technology, under a contract with the National Aeronautics and Space Administration. The authors sincerely appreciate the input from three anonymous reviewers whose helpful suggestions and detailed comments greatly improved this manuscript.

References

Backes, T.M., M.L. Kaplan, R. Schumer, and J.F. Mejia, 2015: A Climatology of the Vertical Structure of Water Vapor Transport to the Sierra Nevada in Cool Season Atmospheric River Precipitation Events. *J. Hydrometeor*, **16**, 1029–1047.

Cordeira J.M., F.M. Ralph and B.J. Moore, 2013: The development and evolution of two atmospheric rivers in proximity to Western North Pacific tropical cyclones in October 2010. *Mon. Wea. Rev.*, **141**, 4234–4255.

Dai, A., T. Qian, and K. E. Trenberth, 2009: Changes in continental freshwater discharge from 1948 to 2004. *J. Climate*, **22**, 2773-2792, doi: 10.1175/2008JCLI2592.1.

Demory, M.-E., P. L. Vidale, M. J. Roberts, P. Berrisford, J. Strachan, R. Schiemann, and M. S. Mizielinski, 2014: The role of horizontal resolution in simulating drivers of the global hydrological cycle. *Clim. Dyn.*, **42**, 2201-2225, doi:10.1007/s00382-013-1924-4.

Dettinger, M. D., F. M. Ralph, T. Das, P. J. Neiman, and D. Cayan, 2011: Atmospheric rivers, floods, and the water resources of California. *Water*, **3**, 455-478.

Environmental Modeling Center, 2003: The GFS Atmospheric Model. NCEP Office Note 442, Global Climate and Weather Modeling Branch, EMC, Camp Springs Maryland. Available online at http://www.emc.ncep.noaa.gov/officenotes/newernotes/on442.pdf. Accessed on June 10, 2017.

Guan, B., N. P. Molotch, D. E. Waliser, E. J. Fetzer, and P. J. Neiman, 2010: Extreme snowfall events linked to atmospheric rivers and surface air temperature via satellite measurements. *Geophys. Res. Lett.*, **37**, L20401, doi:10.1029/2010GL044696.

Guan, B., N. P. Molotch, D. E. Waliser, E. J. Fetzer, and P. J. Neiman, 2013: The 2010/11 snow season in California's Sierra Nevada: Role of atmospheric rivers and modes of large-scale variability. *Water Resour. Res.*, **49**, 6731-6743, doi: 10.1002/wrcr.20537.

Guan, B., and D. E. Waliser, 2015: Detection of atmospheric rivers: Evaluation and application of an algorithm for global studies, *J. Geophys. Res. Atmos*., **120**, 12514–12535, doi:10.1002/2015JD024257.

Kammerer, 1990: Largest rivers in the United States. Report 87-242. U. S. Geological Survey, Report 87-242, available at: http://pubs.usgs.gov/of/1987/ofr87-242/.

Kim, J., D. E. Waliser, P. J. Neiman, B. Guan, J.-M. Ryoo, and G. A. Wick, 2013: Effects of atmospheric river landfalls on the cold season precipitation in California. *Clim. Dyn.*, **40(1-2)**, 465-474, doi:10.1007/s00382-012-1322-3.

Lavers, D. A, R. P. Allan, E. F. Wood, G. Villarini, D. J. Brayshaw, and A. J. Wade, 2011: Winter floods in Britain are connected to atmospheric rivers. *Geophys. Res. Lett.*, **38**, L23803: doi:10.1029/2011GL049783.

Lavers, D. A., G. Villarini, R. P. Allan, E. F. Wood, and A. J. Wade, 2012: The detection of atmospheric rivers in atmospheric reanalyses and their links to British winter floods and the large-scale climatic circulation. *J. Geophys. Res.*, **117**, D20106, doi:10.1029/2012JD018027.

Leung, L. R., and Y. Qian, 2009: Atmospheric rivers induced heavy precipitation and flooding in the western U.S. simulated by the WRF regional climate model. *Geophys. Res. Lett.*, **36**, L03820, doi:10.1029/2008GL036445.

Mahoney, K., D. L. Jackson, P. Neiman, M. Hughes, L. Darby, G. Wick, A. White, E. Sukovich, and R. Cifelli, 2016: Understanding the Role of Atmospheric Rivers in Heavy Precipitation in the Southeast United States. *Mon. Wea. Rev.* **144**: 1617-1632, doi: 10.1175/MWR-D-15-0279.1.

Moore, B. J., P. J. Neiman, F. M. Ralph, F. Barthold, 2012: Physical processes associated with heavy flooding rainfall in Nashville, Tennessee and vicinity during 1-2 May 2012: The role of an atmospheric river and mesoscale convective systems. *Mon. Wea. Rev.*, **140**, 358-378, doi:10.1175/MWR-D-11-00126.1

Neiman, P.J., F.M. Ralph, A.B. White, D.A. Kingsmill, and P.O.G. Persson, 2002: The statistical relationship between upslope flow and rainfall in California's coastal mountains: Observations during CALJET. *Mon. Wea. Rev.*, **130**, 1468-1492.

Neiman, P. J., F. M. Ralph, G. A. Wick, J. Lundquist, and M. D. Dettinger, 2008a: Meteorological characteristics and overland precipitation impacts of atmospheric rivers affecting the West Coast of North America based on eight years of SSM/I satellite observations. *J. Hydrometeor.*, **9**, 22-47.

Neiman, P. J., F. M. Ralph, G. A. Wick, Y.-H. Kuo, T.-K. Wee, Z. Ma, G. H. Taylor, and M. D. Dettinger, 2008b: Diagnosis of an intense atmospheric river impacting the Pacific Northwest: Storm summary and offshore vertical structure observed with COSMIC satellite retrievals. *Mon. Wea. Rev.*, **136**, 4398-4420.

Neiman, P. J., L. J. Schick, F. M. Ralph, M. Hughes, and G. A. Wick, 2011: Flooding in western Washington: The connection to atmospheric rivers. *J. Hydrometeor.*, **12**, 1337-1358.

Neiman, P. J., G. A. Wick, B. J. Moore, F. M. Ralph, J. R. Spackman, and B. Ward, 2014a: An airborne study of an atmospheric river over the subtropical Pacific during WISPAR: Dropsonde budget-box diagnostics and precipitation impacts in Hawaii. *Mon. Wea. Rev.*, **142**, 3199-3223.

Neiman, P.J., F.M. Ralph, B.J. Moore and R. J. Zamora, 2014b: The regional influence of an intense Sierra Barrier Jet and landfalling atmospheric river on orographic precipitation in northern California: A case study. *J. Hydrometeor.*, **15**, 1419-1439.

Pierce, D. W., D. R. Cayan, T. Das, E. P. Maurer, N. L. Miller, Y. Bao, M. Kanamitsu, K. Yoshimura, M. A. Snyder, L. C. Sloan, G. Franco, and M. Tyree, 2013: The key role of heavy precipitation events in climate model disagreements of future annual precipitation changes in California. *J. Climate*, **26**, 5879-5896.

Ralph, F. M., P. J. Neiman, and G. A. Wick, 2004: Satellite and CALJET aircraft observations of atmospheric rivers over the eastern North-Pacific Ocean during the El Nino winter of 1997/98. *Mon. Wea. Rev*., **132**, 1721-1745.

Ralph, F. M., P. J., Neiman and R. Rotunno, 2005: Dropsonde observations in low-level jets over the Northeastern Pacific Ocean from CALJET-1998 and PACJET-2001: Mean vertical-profile and atmospheric-river characteristics. *Mon. Wea. Rev.*, **133**, 889-910.

Ralph, F. M., P. J. Neiman, G. A. Wick, S. I. Gutman, M. D. Dettinger, D. R. Cayan, and A. B. White, 2006: Flooding on California's Russian River: Role of atmospheric rivers. *Geophys. Res. Lett.*, **33**, L13801, doi:10.1029/2006GL026689.

Ralph F. M., P. J. Neiman, G. N. Kiladis, K. Weichman, and D. W. Reynolds, 2011: A multi-scale observational case study of a Pacific atmospheric river exhibiting tropical-extratropical connections and a mesoscale frontal wave. *Mon. Wea. Rev.*, **139**, 1169-1189.

Ralph, F. M., T. Coleman, P.J. Neiman, R. Zamora, and M.D. Dettinger, 2013: Observed impacts of duration and seasonality of atmospheric-river landfalls on soil moisture and runoff in coastal northern California. *J. Hydrometeor.*, **14**, 443-459.

Ralph, F.M, K. A. Prather, D. Cayan, J.R. Spackman, P. DeMott, M. Dettinger, C. Fairall, R. Leung, D. Rosenfeld, S. Rutledge, D. Waliser, A. B. White, J. Cordeira, A. Martin, J. Helly, and J. Intrieri, 2016: CalWater Field Studies Designed to Quantify the Roles of Atmospheric Rivers and Aerosols in Modulating U.S. West Coast Precipitation in a Changing Climate. Bull. Amer. Meteorol. Soc. (in press September 2015).

Rutz, J. J., W. J. Steenburgh, and F. M. Ralph, 2014: Climatological characteristics of atmospheric rivers and their inland penetration over the Western United States. *Mon. Wea. Rev.*, **142**, 905-921.

Seo, K-W., D. E. Waliser, B. Tian, B-M. Kim, S-C. Park, S. Cocke, B-J. Sohn, and M. Ishii, 2012: Evidence of the recent decade change in global fresh water discharge and evapotranspiration revealed by reanalysis and satellite observations. *Asia-Pacific J. Atmos. Sci.*, **48(2)**, 153-158, doi:10.1007/s13143-012-0015-5.

Stohl, A., C. Forster, and H. Sodemann, 2008: Remote sources of water vapor forming precipitation on the Norwegian west coast at 60°N - A tale of hurricanes and an atmospheric river. *J. Geophys. Res.*, **113**, D05102, doi:10.1029/2007JD009006.

Trenberth, K. E., J. T. Fasullo, and J. Mackaro, 2011: Atmospheric moisture transports from ocean to land and global energy flows in reanalyses. *J. Climate*, **24**, 4907-4924.

Viale, M., and M. N. Nunez, 2011: Climatology of winter orographic precipitation over the subtropical central Andes and associated synoptic and regional characteristics. *J. Hydrometeor.*, **12**, 481-507.

Waliser, D.W., et al., 2012: The "Year" of Tropical Convection (May 2008 to April 2010): Climate variability and weather highlights, *Bull. Amer. Meteor. Soc.*, **93**, 1189-1218, doi:10.1175/2011BAMS3095.1.

Wentz, F. J., K.A. Hilburn, D.K. Smith, 2012: Remote Sensing Systems DMSP SSM/I Daily Environmental Suite on 0.25 deg grid, Version 7. Remote Sensing Systems, Santa Rosa, CA. Available online at www.remss.com/missions/ssmi. Accessed 21-Nov-2016.

White, A.B., M.L. Anderson, M.D. Dettinger, F.M. Ralph, A. Hinojosa, D.R. Cayan, R.K. Hartman, D.W. Reynolds, L.E. Johnson, T.L. Schneider, R. Cifelli, Z. Toth, S.I. Gutman, C.W. King, F. Gehrke, P.E. Johnston, C. Walls, D. Mann, D.J. Gottas and T. Coleman, 2013: A 21st century California observing network for monitoring extreme weather events. *J. Atmos. Ocean. Technol.*, **30**, 1585-1603.

Wick G. A., P. J. Neiman, and F. M. Ralph, 2013: Description and validation of an automated objective technique for identification and characterization of the integrated water vapor signature of atmospheric rivers. *IEEE Trans. Geosci. Remote Sens.*, **51**, 2166-2176.

Wohl, E. E., 2007: Hydrology and Discharge. *Large Rivers: Geomorphology and Management*, Ed. A. Gupta, John Wiley & Sons, doi:10.1002/9780470723722.ch3.

Zhu, Y., and R. E. Newell, 1998: A proposed algorithm for moisture fluxes from atmospheric rivers. *Mon. Wea. Rev.*, **126**, 725-735.

	Date (UTC at initial dropsonde)	Campaign	Aircraft	Number of Usable Sondes
1	25-Jan-1998	CALJET	NOAA P-3	25
2	24-Mar-2005	Ghostnets	NOAA P-3	33
3	26 Mar 2005	Ghostnets	NOAA P-3	23
4	11-Feb-2011	WISPAR	NASA Global Hawk	19
5	03-Mar-2011	WISPAR	NOAA G-IV	42
6	03-Mar-2011	WISPAR	NASA Global Hawk	59
7	09-Mar-2011	WISPAR	NASA Global Hawk	56
8	07-Feb-2014	CalWater2 - Pre	NOAA G-IV	23
9	08-Feb-2014	CalWater2 - Pre	NOAA G-IV	29
10	11-Feb-2014	CalWater2 - Pre	NOAA G-IV	37
11	12-Feb-2014	CalWater2 - Pre	NOAA G-IV	15
12	13-Feb-2014	CalWater2 - Pre	NOAA G-IV	23
13	14-Feb-2014	CalWater2 - Pre	NOAA G-IV	4
14	15-Feb-2014	CalWater2 - Pre	NOAA G-IV	14
15	18-Feb-2014	CalWater2 - Pre	NOAA G-IV	14
16	19-Feb-2014	CalWater2 - Pre	NOAA G-IV	12
17	21-Feb-2014	CalWater2 - Pre	NOAA G-IV	17
18	22-Feb-2014	CalWater2 - Pre	NOAA G-IV	4
19	25-Feb-2014	CalWater2 - Pre	NOAA G-IV	4
20	15-Jan-2015	CalWater2	NOAA G-IV	24
21	17-Jan-2015	CalWater2	NOAA G-IV	29
22	22-Jan-2015	CalWater2	NOAA G-IV	13
23	24-Jan-2015	CalWater2	NOAA G-IV	23
24	05-Feb-2015	CalWater2	NOAA G-IV	8
25	06-Feb-2015	CalWater2	NOAA G-IV	29
26	08-Feb-2015	CalWater2	NOAA G-IV	31
27	14-Feb-2015	CalWater2	NOAA G-IV	40
28	20-Feb-2015a	CalWater2	NOAA G-IV	37
29	20-Feb-2015b	CalWater2	NOAA G-IV	28
30	22-Feb-2015	CalWater2	NOAA G-IV	30
31	24-Feb-2015	CalWater2	NOAA G-IV	35
32	13-Feb-2016	CalWater2	USAF C-130 (H)	51
33	13-Feb-2016	CalWater2	USAF C-130 (M)	47
34	15-Feb-2016	CalWater2	USAF C-130 (M)	41
35	15-Feb-2016	CalWater2	USAF C-130 (H)	39
36	21-Feb-2016	CalWater2	USAF C-130 (M)	37
37	21-Feb-2016	CalWater2	USAF C-130 (H)	57
			TOTAL:	**1052**

Table 1. List of research flights used in this study. Included in the table are the number of dropsondes within the criteria noted in the main text. CALJET = California Land-falling Jets Experiment; WISPAR = Winter Storms and Pacific Atmospheric Rivers Experiment. USAF C-130 flights were flown out of Hickam AFB (H) or McChord AFB, CA (M).

Case #	Date	Aircraft	Start/End Time	Central Longitude	Central Latitude	No. of Sondes@	Mean Dir.	IWV_{MAX} (mm)	IVT_{MAX} (kg m^{-1} s^{-1})	$TIVT_a$ (10^8 kg s^{-1})	$Width_a$ (km)	$TIVT_b$ (10^8 kg s^{-1})	$Width_b$ (km)
	Subtropical												
1	25-Mar-2005	P-3	0040-0300Z	156.2°W	27.2°N	16	233	41.2	674	4.26	1196	3.96	1016
2	12-Feb-2011	G-Hawk	0558-0726Z	145.9°W	27.7°N	9	237	41.0	585	2.37	811	1.77	415
3	04-Mar-2011	G-IV	0003-0302Z	163.4°W	23.0°N	17	220	48.9	725	4.85	1539	4.24	849
6	08-Feb-2014	G-IV	2243-2338Z	139.3°W	31.0°N	9	230	41.7	1029	3.44	602	3.56	611
10	19-Feb-2014	G-IV	2312-0158Z	151.7°W	27.5°N	11	203	39.6	314	3.54	1802	1.33	477
15	14-Feb-2015	G-IV	1823-1928Z	152.3°W	24.2°N	11	229	46.1	1204	6.62	846	6.87	917
16	20-Feb-2015	G-IV	0012-0154Z	156.7°W	27.0°N	13	240	41.7	861	5.19	964	5.63	1092
17	22-Feb-2015	G-IV	2152-2330Z	160.8°W	31.0°N	17	232	39.1	926	6.94	1334	6.30	1026
21	21-Feb-2016	C-130	2037-0004Z	149.6°W	29.1°N	24	208	32.7	942	7.08	1202	8.33	1354
Mean (subtropical cases)						**14**	**226**	**41.3**	**807**	**4.92**	**1144**	**4.67**	**862**
Standard Deviation						**4.6**	**12**	**4.3**	**249**	**1.59**	**359**	**2.19**	**291**
	Mid-latitude												
4	04-Mar-2011	G-Hawk	1102-1340Z	134.7°W	41.5°N	10	231	18.1	531	NA*	NA*	2.46	687
5	09-Mar-2011	G-Hawk	2240-0022Z	131.1°W	40.4°N	15	226	25.0	622	1.92	382	3.26	723
7	11-Feb-2014	G-IV	1903-2124Z	134.0°W	42.1°N	23	232	37.4	1296	7.94	1035	8.05	1067
8	12-Feb-2014	G-IV	1734-1903Z	125.5°W	40.8°N	14	245	32.0	636	3.21	808	2.80	619
9	13-Feb-2014	G-IV	1833-2058Z	133.0°W	42.5°N	21	220	33.2	789	4.39	733	6.90	1371
11	15-Jan-2015	G-IV	2114-2222Z	127.3°W	41.8°N	9	219	27.4	733	3.21	639	3.45	692
12	17-Jan-2015	G-IV	2245-0030Z	130.2°W	41.6°N	10	236	28.4	831	4.17	603	6.11	1154
13	24-Jan-2015	G-IV	2148-2254Z	139.6°W	38.2°N	12	203	29.9	607	2.58	534	3.74	868

14	08-Feb-2015	G-IV	1328-1448Z	124.6°W	34.9°N	11	216	34.8	938	4.35	774	5.96	1054
18	13-Feb-2016	C-130	2055-2250Z	152.7°W	40.0°N	19	229	29.7	798	3.50	515	5.16	963
19	14-Feb-2016	C-130	2341-0158Z	142.0°W	43.0°N	23	241	32.5	954	5.93	875	6.82	1143
20	15-Feb-2016	C-130	2107-2221Z	130.5°W	46.4°N	10	242	23.0	554	1.18	222	2.22	514
Mean (midlatitude cases)						**15**	**228**	**29.3**	**774**	**3.85**	**647**	**4.74**	**905**
Standard Deviation						**5**	**12**	**5.1**	**207**	**1.79**	**221**	**1.91**	**250**
Overall Mean						**14.5**	**227**	**34.4**	**788**	**4.33**	**871**	**4.71**	**886**
Overall Standard Deviation						**4.9**	**12**	**7.6**	**227**	**1.78**	**382**	**2.04**	**269**

* No dropsondes satisfied the IWV>20 mm threshold; @Number of sondes in AR transect

Table 2. Flight information and derived atmospheric properties from the 17 AR transects used in this study. The width and total integrated vapor transport (TIVT) of each AR were calculated using both IWV (subscript a) and IVT (subscript b) critical thresholds of 20 mm and 250 kg m^{-1} s^{-1}, respectively. The first column is the case number, which is chronological. The date corresponds to the midpoint of each transect. The mean direction is defined using the vertically integrated (from surface to top of sounding) u- and v-components of IVT. The cases are separated into those from the subtropics (centered from roughly 23-33^0 N) and those from the midlatitudes (centered from roughly 33-43^0 N), and statistics of each subset are provided. The bottom two rows contain the mean and standard deviations for all 17 transects.

	Mean Flow Rate		
	10^9 m^3 day^{-1}	10^6 acre-feet day^{-1}	Multiplier
Average AR in this study	39.7	32.2	1 AR = X rivers
Largest AR in this study	71.7	58.2	
Amazon River	15.1	12.3	2.6
Congo River	3.6	2.9	11.0
Yangtze River	3.0	2.5	13.2
Mississippi River	1.5	1.2	27.4
Nile River	0.3	0.2	159

Table 3. Comparison of mean flow rates between the observed ARs in this study and major river systems. Mean river flow rates from Wohl (2007) except for Mississippi River which was taken from Kammerer (1990).

Figure Captions

Figure 1. Composite SSMI satellite imagery of IWV during AR events 1-12 listed in Table 2. Composites formed using available SSMI data within +/- 16 hours of transect time. The white lines represent the approximate location of each AR transect. The image times (upper right corner of each panel) were selected to correspond to as close as possible to the midpoint of each transect. The total vapor transport within each AR using both IWV ($TIVT_1$) and IVT ($TIVT_2$) critical thresholds are listed above each panel. White areas denote either land pixels or missing data. Some of the IWV imagery contains artifacts that result from the blending of data +/- 16

hours of the transect time. SSMI data produced by Remote Sensing Systems and accessed at www.remss.com.

Figure 2. Same as Figure 1, except for AR events 13-21 listed in Table 2.

Figure 3. IWV (left column) and IVT (right column) calculated along each transect listed in Table 2. Transects are grouped by location: subtropical (top row) and midlatitude (bottom row). The horizontal distance scale is referenced to the dropsonde location with the largest value of IWV or IVT in each transect. Transects are oriented with the cold end (generally towards the northwest) located on the left side of the plots. The horizontal black lines represent the critical IWV and IVT thresholds (see text) used to identify the presence of an AR.

Figure 4. Location of the dropsonde transects listed in Table 1 (transect numbers, per Table 1, are shown). The background image denotes weekly AR frequency calculated using the AR Detection Tool of Wick et al (2013) applied during the 2003-2012 cool seasons (November-February). AR frequency data west of 160°W was not available.

Figure 5. AR composite from 21 cases observed over the Eastern North Pacific Ocean. Gridded plan view composite derived from gridded GFS reanalysis data with mean central position of all 21 cases denoted by white dot and composite. Top panel contains composite IWV (mm - color fill), IVT direction (vectors) and magnitude (kg m^{-1} s^{-1} - dashed black contours at intervals of 50 kg m^{-1} s^{-1} and vector length) and bottom panel shows composite precipitation rate. In both panels the composite MSLP (hPa) is denoted by the thin sold contours.

Figure 6. AR composite cross section based on dropsonde data from the 21 cases observed over the Eastern North Pacific Ocean derived by normalizing the horizontal width of each transect to match the mean width of 860 km (baseline shown as purple line in Figure 4). Top panel contains observed composite vertical cross section. Color contours represent the magnitude of the local horizontal water vapor transport, which has been normalized to match the mean TIVT of all 21 ARs. Mean wind speed (dashed white contours; >40 m s^{-1} hatched). Freezing level (solid white line), vertical position of H75, and 925 hPa wind speed and direction (barbs = 5 m s^{-1} and half-barbs = 2.5 m s^{-1}) are also shown. Horizontal layers containing 75%, 20%, 4% and 1% of the TIVT are marked. Bottom panel shows mean cross-AR profiles of IVT and IWV.

Figure 7. Same as Figure 5, except for the 9 sub-tropical cases.

Figure 8. Same as Figure 6, except for the 9 sub-tropical cases.

Figure 9. Same as Figure 5, except for the 12 mid-latitude cases.

Figure 10. Same as Figure 6, except for the 12 mid-latitude cases.

Figure 11. Comparison of the maximum IVT (IVT_{MAX}) and maximum IWV (IWV_{MAX}) to the total horizontally integrated IVT (TIVT) for each of the 21 cases listed in Table 1. The correlation between these values of IVT_{MAX} and TIVT is 0.83 and the correlation between IWV_{MAX} and TIVT is 0.20.

Figure 12. Illustration showing how spacing between dropsondes was varied for resolution experiments using AR event 9 as an example. The white dots represent the locations of dropsondes. The original spacing is shown in (a). The spacing for the experiments with increased spacing are shown in panel (b) 2X, (c) 4X, and (d) 8X. The background color fill shows IWV from SSMI satellite measurements as described in Figure 1.

Figure 13. Results from experiments examining the sensitivity of calculated TIVT to the spacing between dropsondes. The difference in TIVT between the control case (ΔTIVT) is shown as a function of the normalized dropsonde spacing (spacing relative to each respective control case; mean dropsonde spacing in these events varied from 63 to 95 km with a mean of 80 km). The circle markers show results from each individual case considered while the vertical bars show the mean across the cases.

Figure 14. Difference in IWV (left column) and IVT (right column) between dropsondes and GFS analysis products along 14 of the 21 AR transects.. The thick black line in each panel represents the average over all transects. Transects are grouped by location: subtropical (top row) and midlatitude (bottom row). The horizontal distance scale is referenced to the dropsonde location with the largest value of IWV or IVT in each transect. Transects are oriented with the cold end (generally towards the northwest) located on the left side of the plots.

Figure 15. Comparisons of TIVT across 14 AR transects from dropsondes and GFS analysis products. Left panel shows comparison between TIVT computed through the entire atmospheric

column. The middle panel shows a comparison of vertical profile of TIVT calculated within 50hPa layers from the dropsondes (solid lines) and GFS analysis (dashed lines). The results are normalized by the respective TIVT value calculated over the entire column. The thin lines represent individual subtropical (blue lines) and mid-latitude (red lines) transects while the thick lines represent an average of all transects in each region. The difference between dropsonde and GFS calculated values is shown in the right panel with thin lines denoting individual transects and the thick lines representing the average of all transects in each region.

Figure 16. Schematic summary of the structure and strength of an atmospheric river based on dropsonde measurements analyzed in this study, and on corresponding reanalyses that provide the plan-view context. (a) Plan view including parent low pressure system, and associated cold, warm, stationary and warm-occluded surface fronts. IVT is shown by color fill (magnitude, kg m^{-1} s^{-1}) and direction in the core (white arrow). Vertically integrated water vapor (IWV, cm) is contoured. A representative length scale is shown. The position of the cross-section shown in panel (b) is denoted by the dashed line A-A'. (b) Vertical cross-section perspective, including the core of the water vapor transport in the atmospheric river (orange contours and color fill) and the pre-cold-frontal low-level jet (LLJ), in the context of the jet-front system and tropopause. Water vapor mixing ratio (green dotted lines, g kg^{-1}) and cross-section-normal isotachs (blue contours, m s^{-1}) are shown. Magnitudes of variables represent an average mid-latitude atmospheric river with lateral boundaries defined using the IVT threshold of 250 kg m^{-1} s^{-1}. Depth corresponds to the altitude below which 75% of IVT occurs. Adapted primarily from Ralph et al. 2004 and Cordeira et al. 2013.

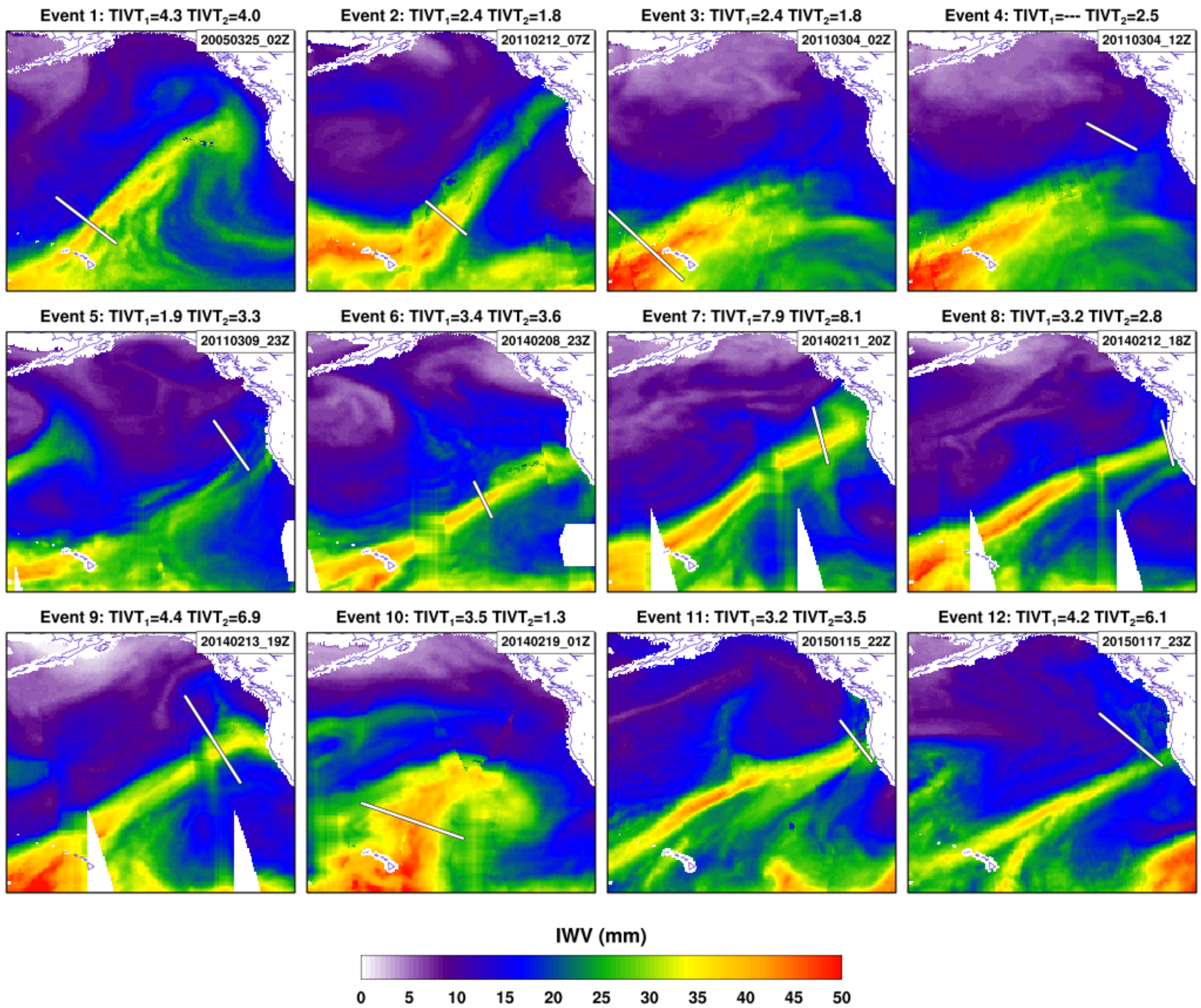

Figure 1. Composite SSMI satellite imagery of IWV during AR events 1-12 listed in Table 2. Composites formed using available SSMI data within +/- 16 hours of transect time. The white lines represent the approximate location of each AR transect. The image times (upper right corner of each panel) were selected to correspond to as close as possible to the midpoint of each transect. The total vapor transport within each AR using both IWV ($TIVT_1$) and IVT ($TIVT_2$) critical thresholds are listed above each panel. White areas denote either land pixels or missing data. Some of the IWV imagery contains artifacts that result from the blending of data +/- 16 hours of the transect time. SSMI data produced by Remote Sensing Systems and accessed at www.remss.com.

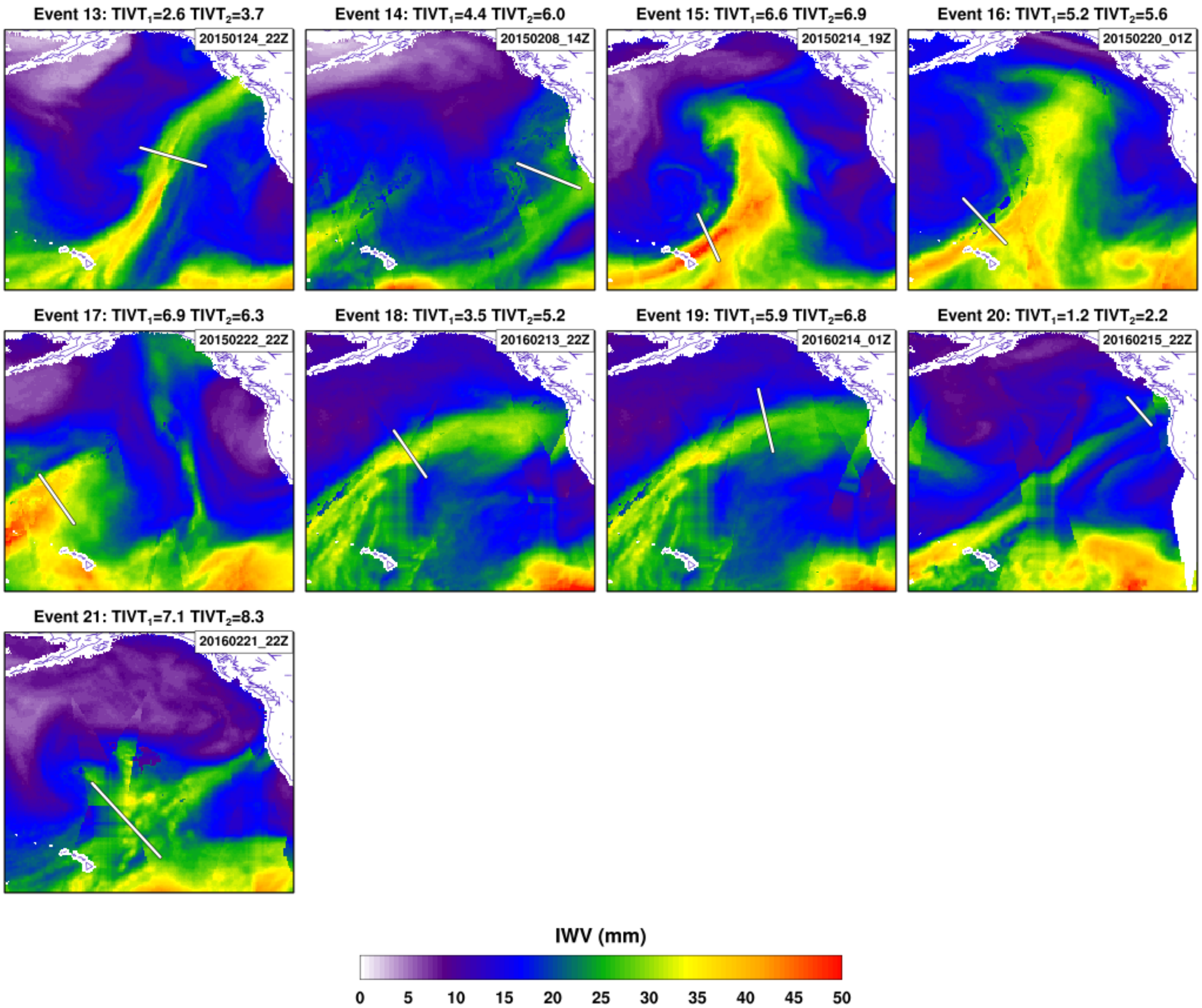

Figure 2. Same as Figure 1, except for AR events 13-21 listed in Table 2.

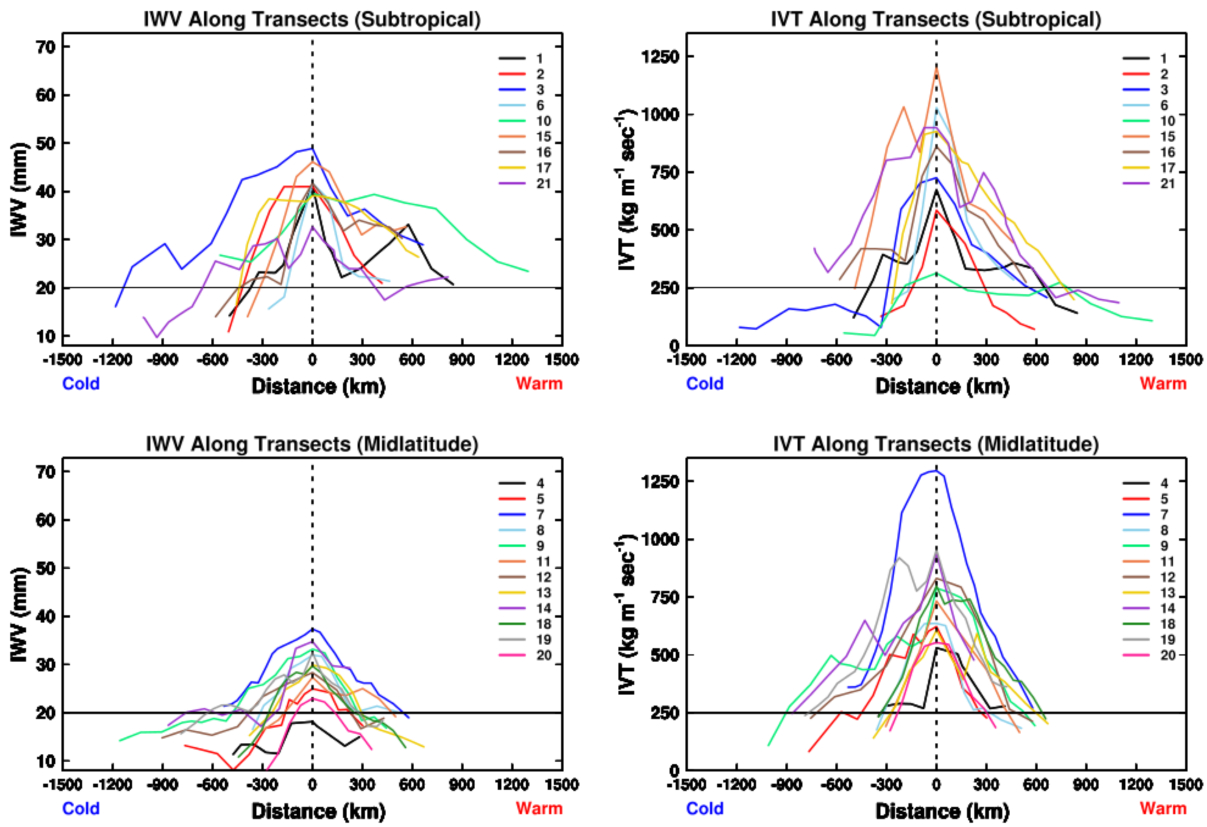

Figure 3. IWV (left column) and IVT (right column) calculated along each transect listed in Table 2. Transects are grouped by location: subtropical (top row) and midlatitude (bottom row). The horizontal distance scale is referenced to the dropsonde location with the largest value of IWV or IVT in each transect. Transects are oriented with the cold end (generally towards the northwest) located on the left side of the plots. The horizontal black lines represent the critical IWV and IVT thresholds (see text) used to identify the presence of an AR.

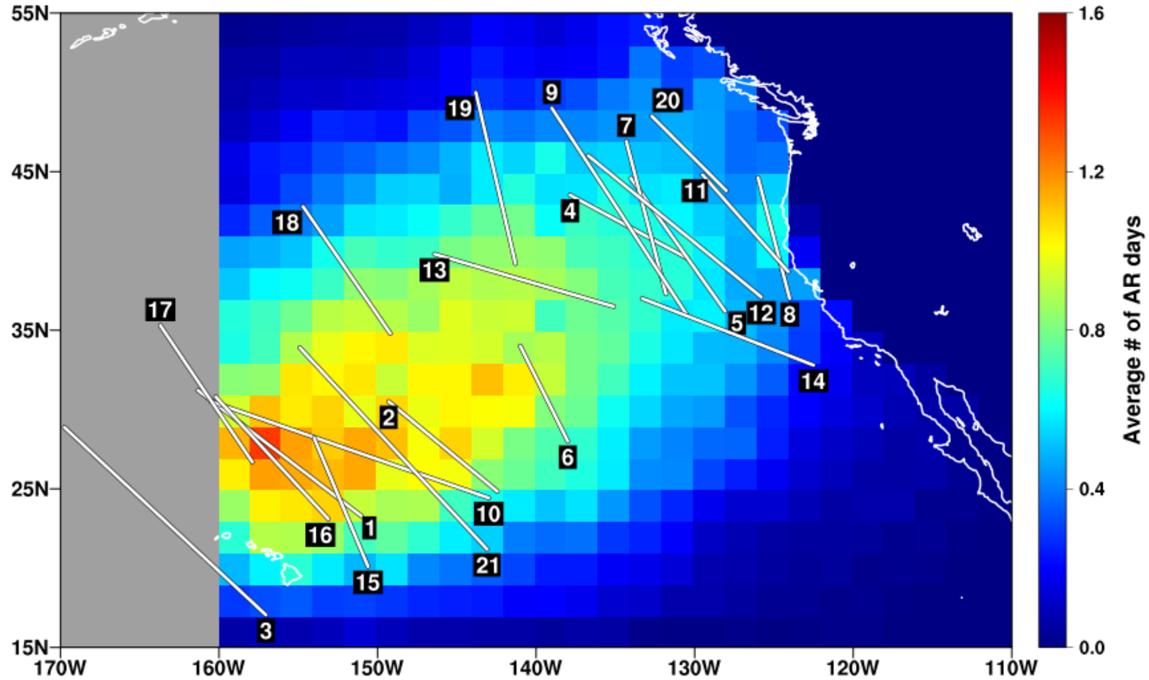

Figure 4. Location of the dropsonde transects listed in Table 1 (transect numbers, per Table 1, are shown). The background image denotes weekly AR frequency calculated using the AR Detection Tool of Wick et al (2013) applied during the 2003-2012 cool seasons (November-February). AR frequency data west of 160°W was not available.

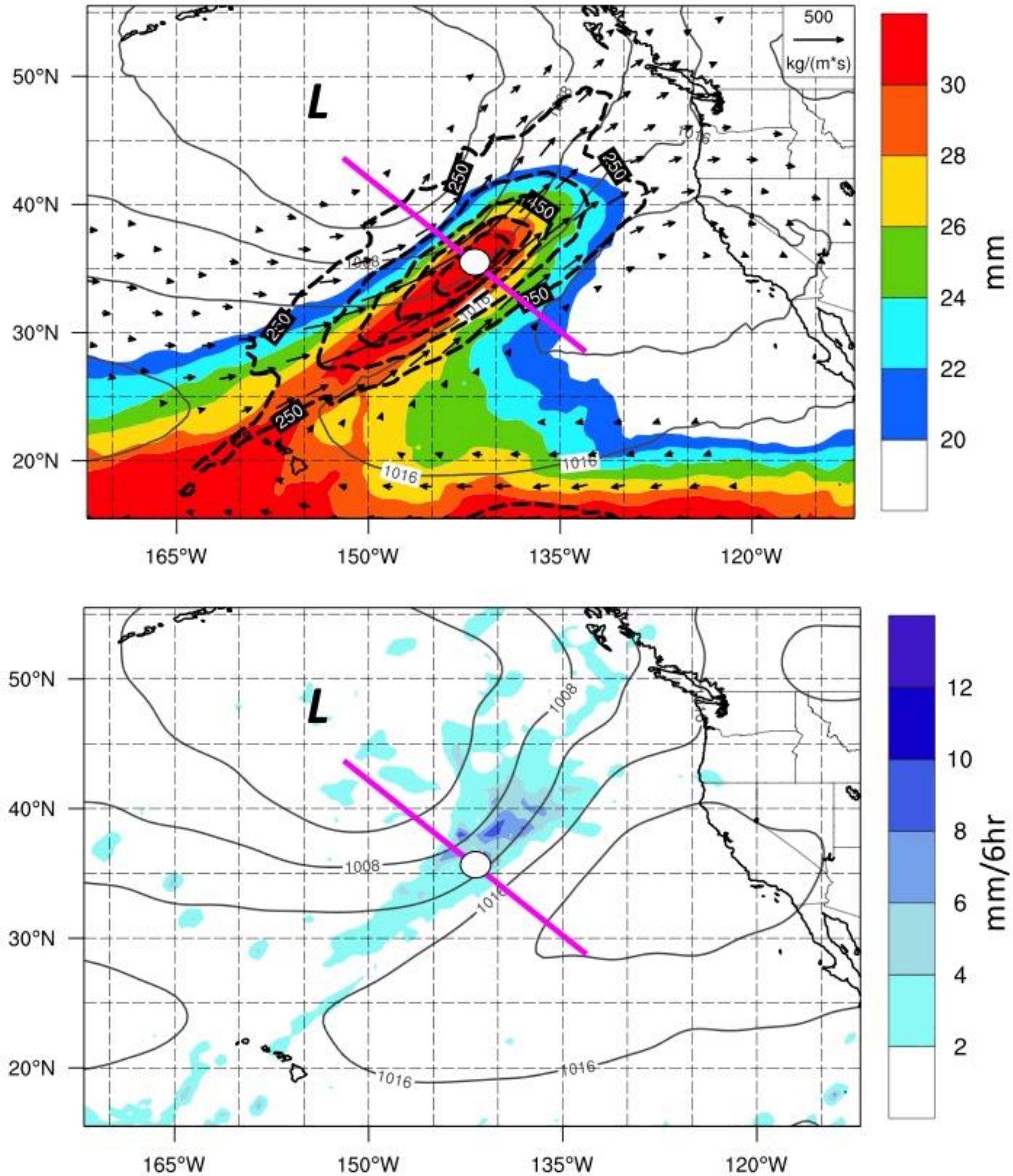

Figure 5. AR composite from 21 cases observed over the Eastern North Pacific Ocean. Gridded plan view composite derived from gridded GFS reanalysis data with mean central position of all 21 cases denoted by white dot and composite. Top panel contains composite IWV (mm - color

fill), IVT direction (vectors) and magnitude (kg m^{-1} s^{-1} - dashed black contours at intervals of 50 kg m^{-1} s^{-1} and vector length) and bottom panel shows composite precipitation rate. In both panels the composite MSLP (hPa) is denoted by the thin sold contours.

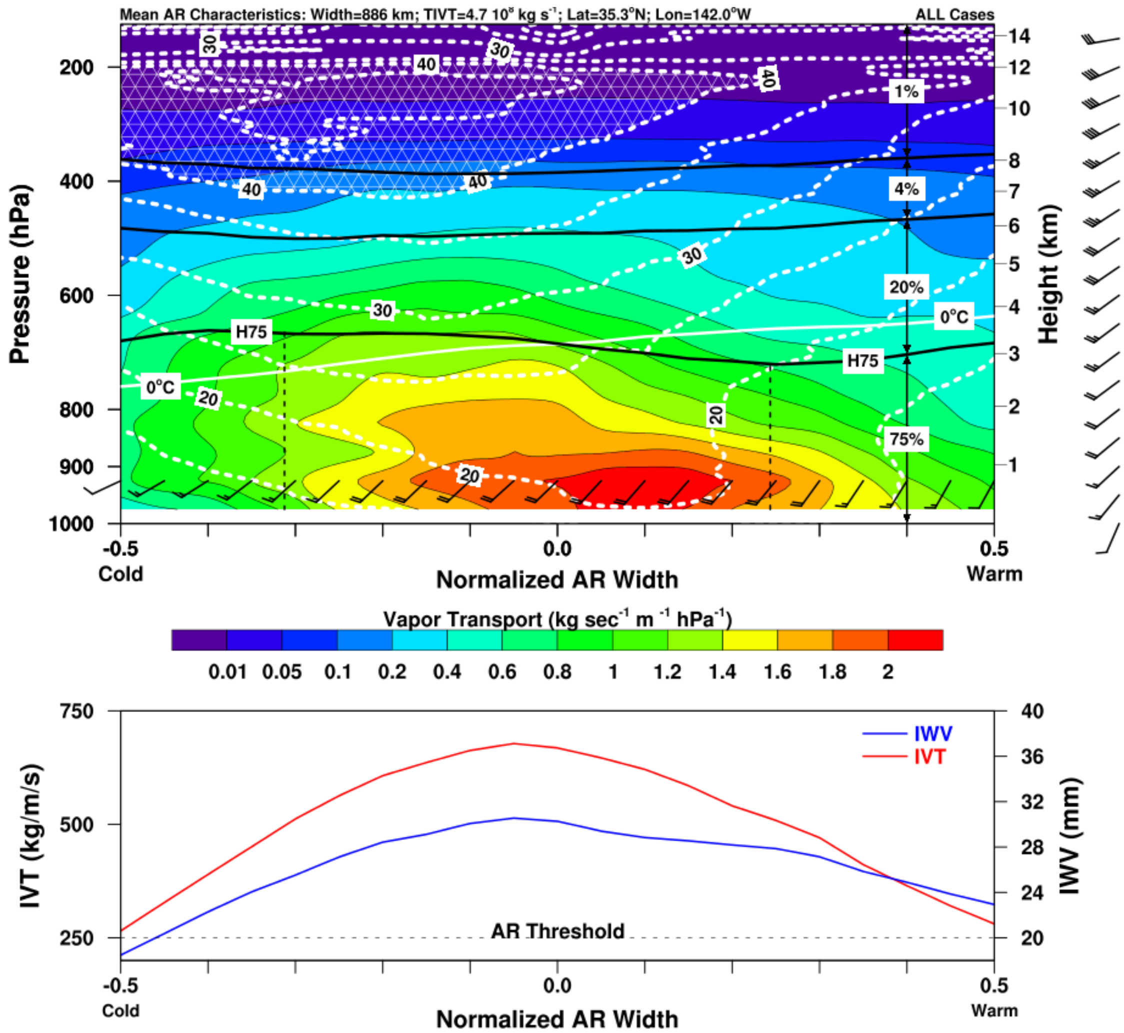

Figure 6. AR composite cross section based on dropsonde data from the 21 cases observed over the Eastern North Pacific Ocean derived by normalizing the horizontal width of each transect to match the mean width of 860 km (baseline shown as purple line in Figure 4). Top panel contains observed composite vertical cross section. Color contours represent the magnitude of the local horizontal water vapor transport, which has been normalized to match the mean TIVT of all 21 ARs. Mean wind speed (dashed white contours; >40 m s^{-1} hatched). Freezing level (solid white line), vertical position of H75, and 925 hPa wind speed and direction (barbs = 5 m s^{-1} and half-

barbs = 2.5 m s^{-1}) are also shown. Horizontal layers containing 75%, 20%, 4% and 1% of the TIVT are marked. Bottom panel shows mean cross-AR profiles of IVT and IWV.

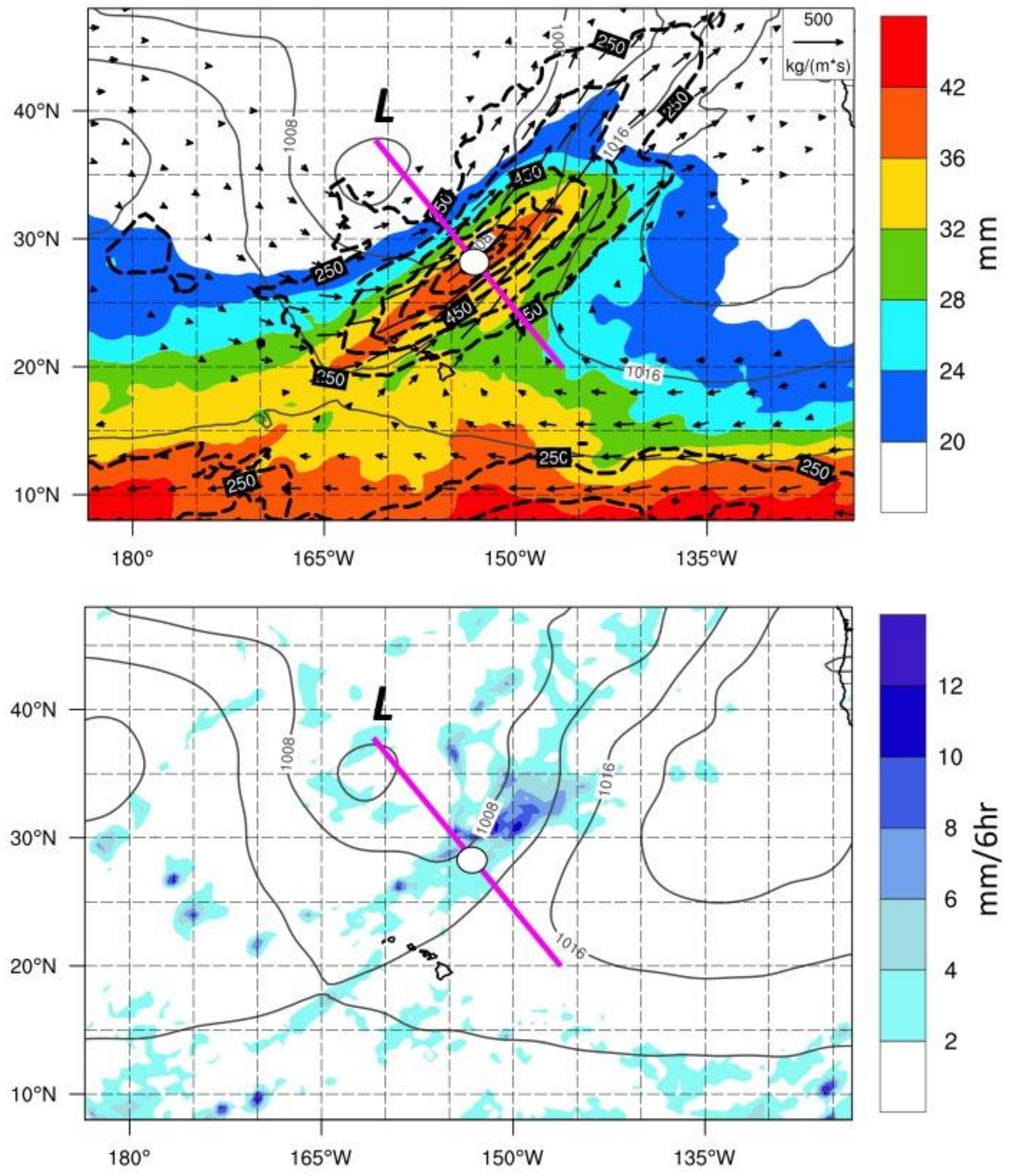

Figure 7. Same as Figure 5, except for the 9 sub-tropical cases.

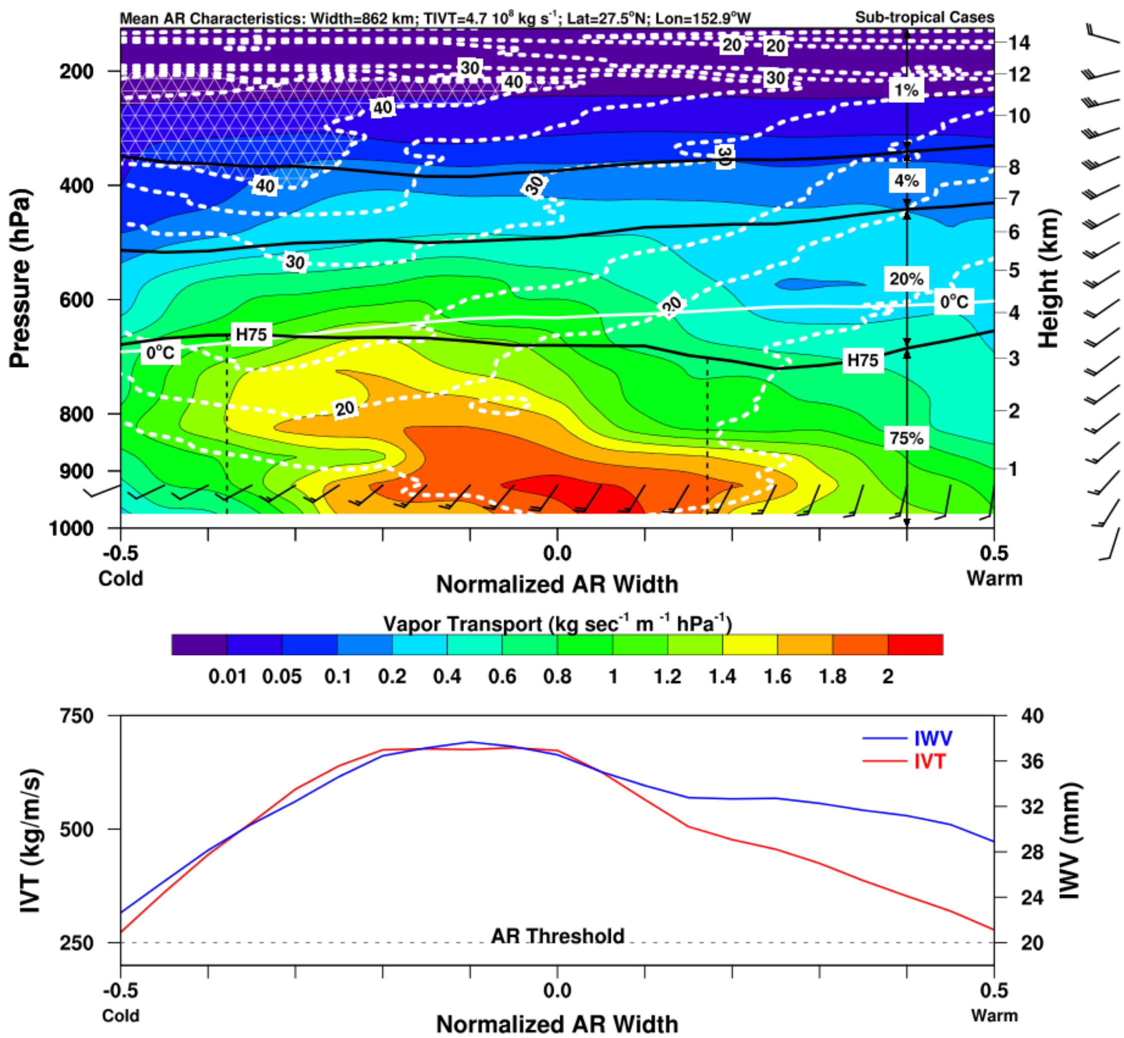

Figure 8. Same as Figure 6, except for the 9 sub-tropical cases.

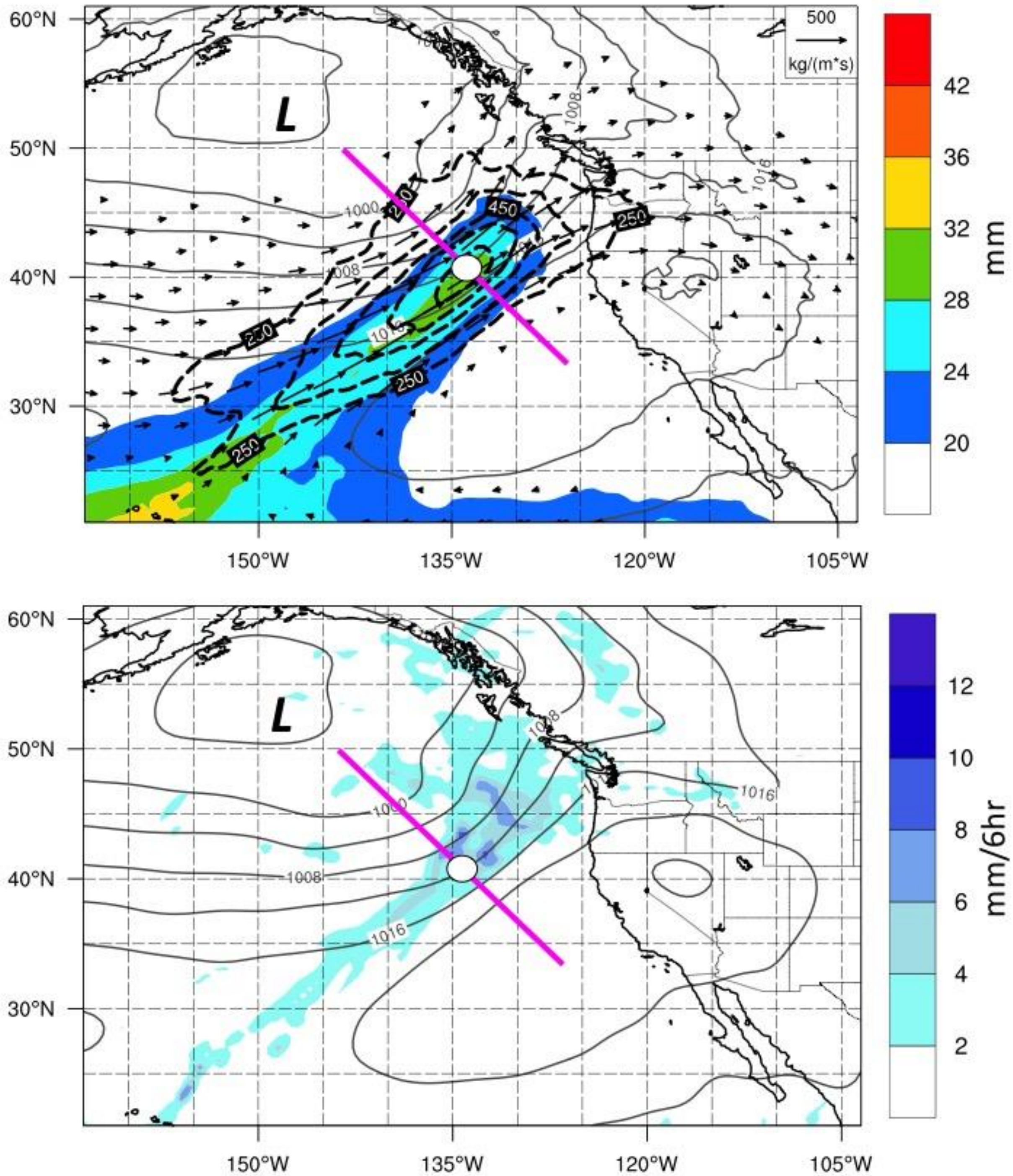

Figure 9. Same as Figure 5, except for the 12 mid-latitude cases.

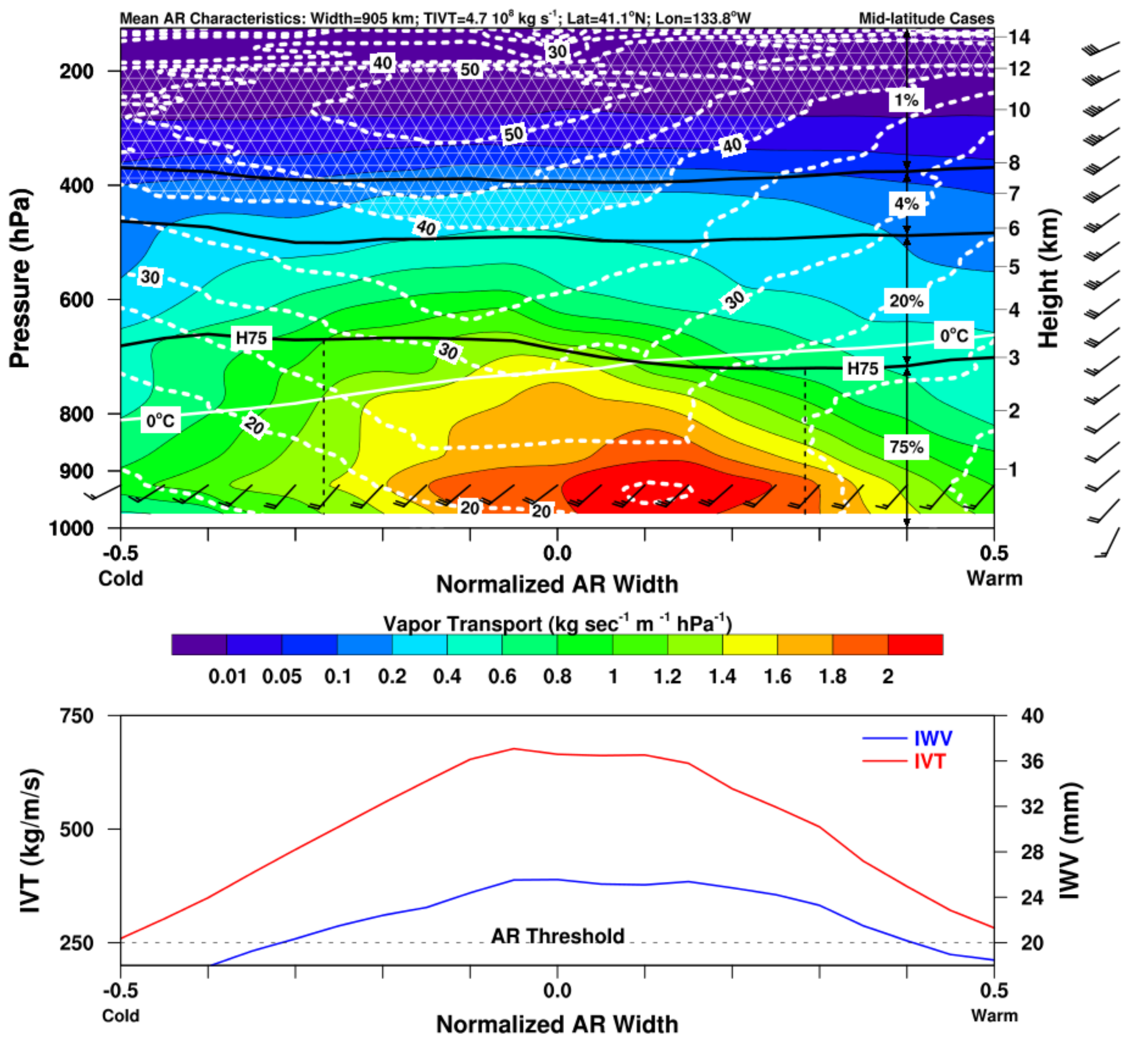

Figure 10. Same as Figure 6, except for the 12 mid-latitude cases.

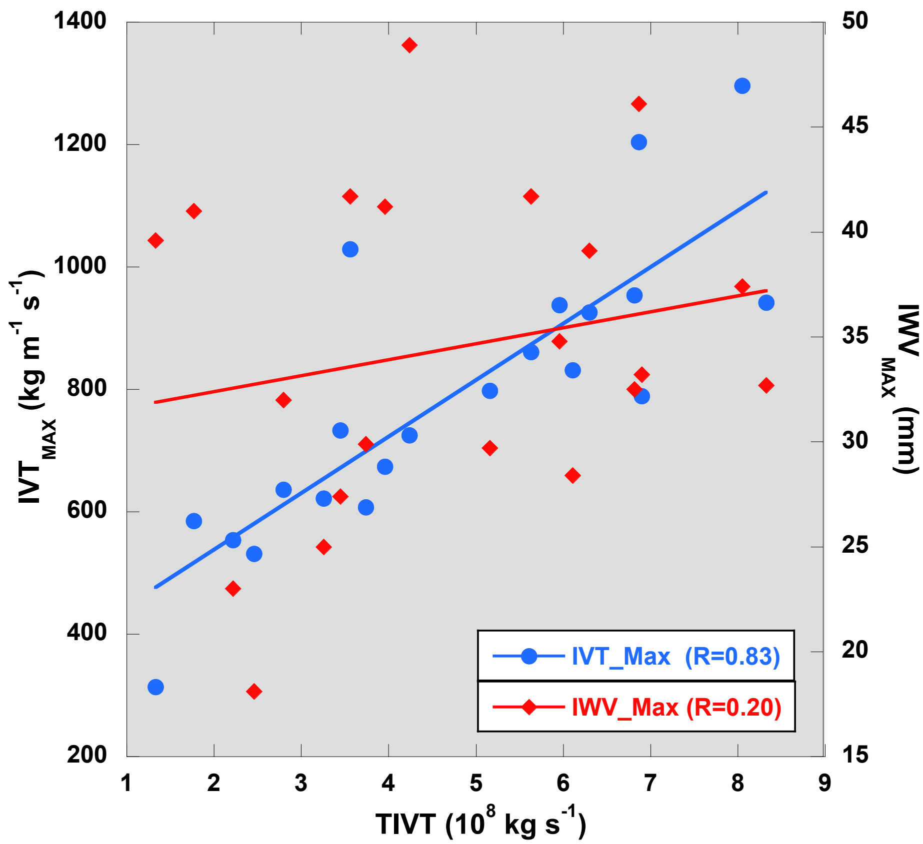

Figure 11. Comparison of the maximum IVT (IVT_{MAX}) and maximum IWV (IWV_{MAX}) to the total horizontally integrated IVT (TIVT) for each of the 21 cases listed in Table 1. The correlation between these values of IVT_{MAX} and TIVT is 0.83 and the correlation between IWV_{MAX} and TIVT is 0.20.

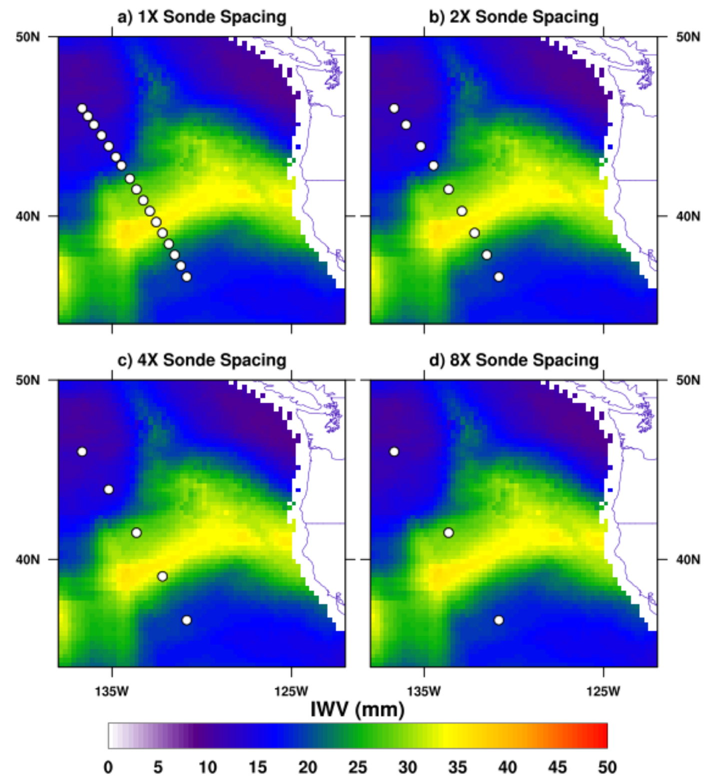

Figure 12. Illustration showing how spacing between dropsondes was varied for resolution experiments using AR event 9 as an example. The white dots represent the locations of dropsondes. The original spacing is shown in (a). The spacing for the experiments with increased spacing are shown in panel (b) 2X, (c) 4X, and (d) 8X. The background color fill shows IWV from SSMI satellite measurements as described in Figure 1.

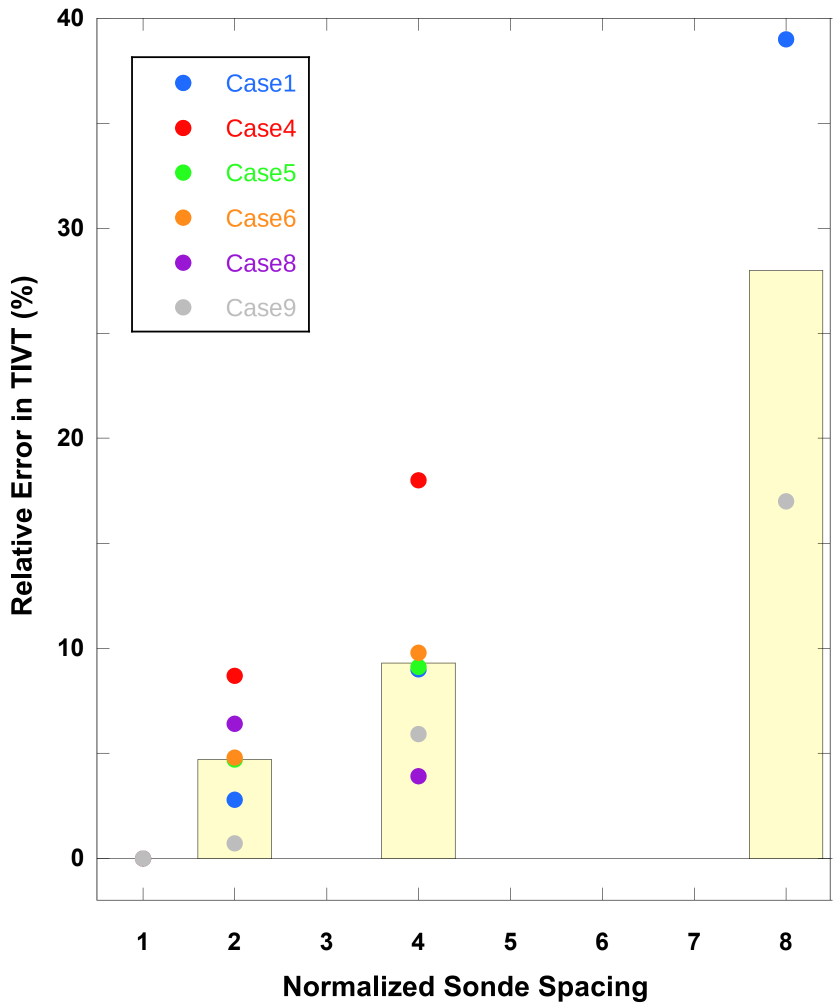

Figure 13. Results from experiments examining the sensitivity of calculated TIVT to the spacing between dropsondes. The difference in TIVT between the control case (ΔTIVT) is shown as a function of the normalized dropsonde spacing (spacing relative to each respective control case; mean dropsonde spacing in these events varied from 63 to 95 km with a mean of 80 km). The circle markers show results from each individual case considered while the vertical bars show the mean across the cases.

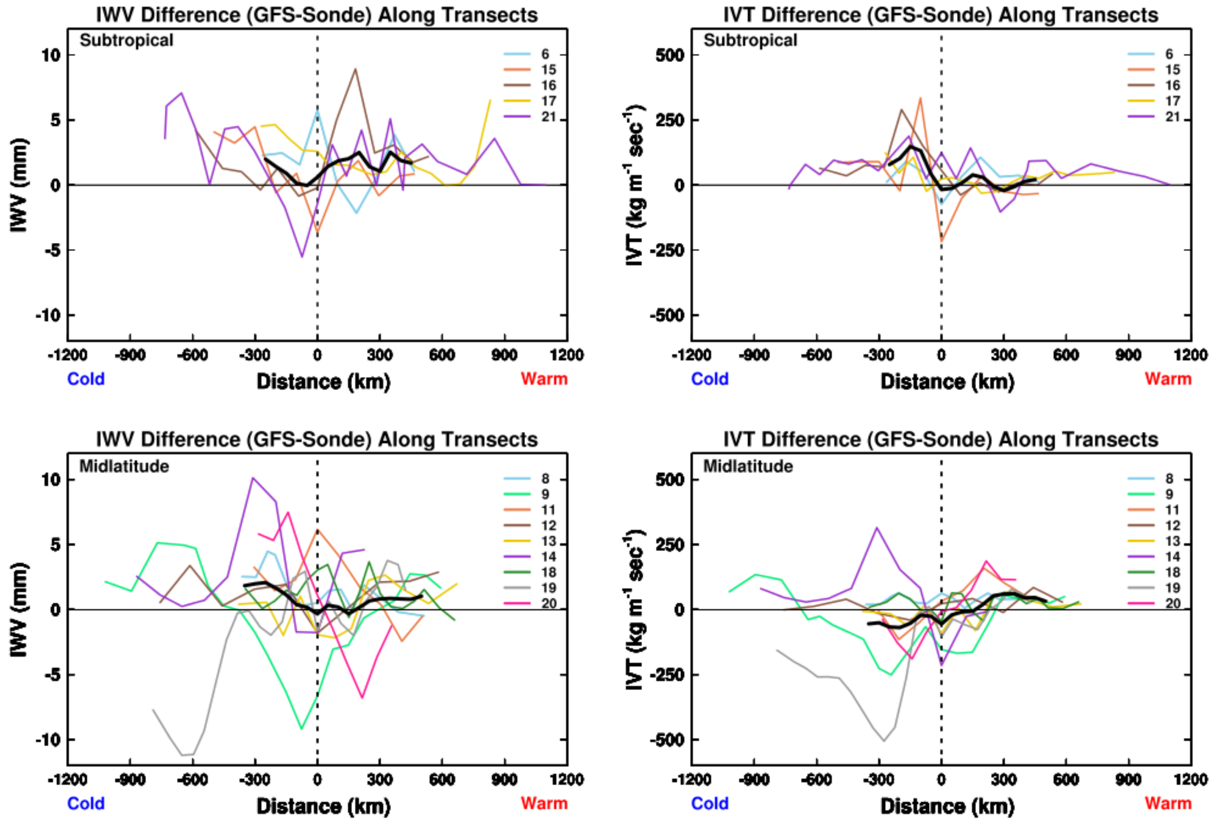

Figure 14. Difference in IWV (left column) and IVT (right column) between dropsondes and GFS analysis products along 14 of the 21 AR transects. The thick black line in each panel represents the average over all transects. Transects are grouped by location: subtropical (top row) and midlatitude (bottom row). The horizontal distance scale is referenced to the dropsonde location with the largest value of IWV or IVT in each transect. Transects are oriented with the cold end (generally towards the northwest) located on the left side of the plots.

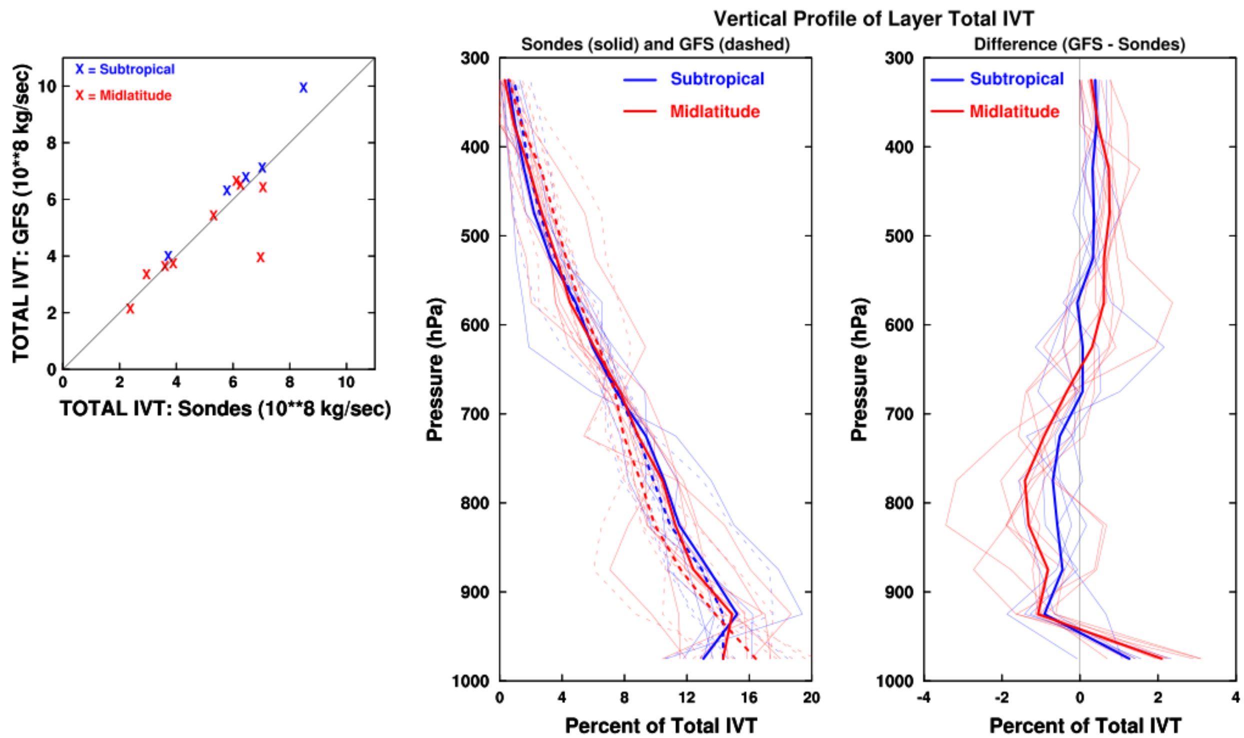

Figure 15. Comparisons of TIVT across 14 AR transects from dropsondes and GFS analysis products. Left panel shows comparison between TIVT computed through the entire atmospheric column. The middle panel shows a comparison of vertical profile of TIVT calculated within 50hPa layers from the dropsondes (solid lines) and GFS analysis (dashed lines). The results are normalized by the respective TIVT value calculated over the entire column. The thin lines represent individual subtropical (blue lines) and mid-latitude (red lines) transects while the thick lines represent an average of all transects in each region. The difference between dropsonde and GFS calculated values is shown in the right panel with thin lines denoting individual transects and the thick lines representing the average of all transects in each region.

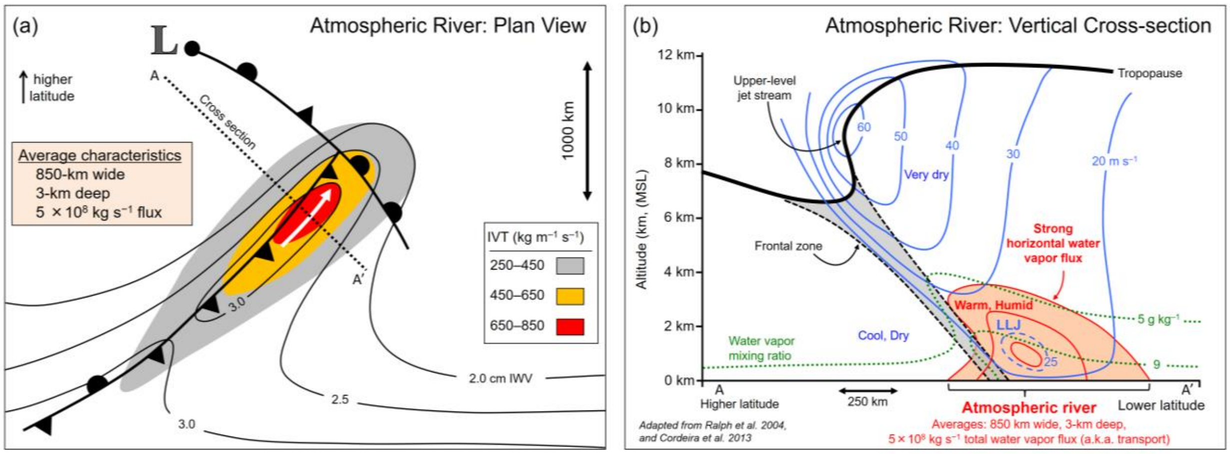

Figure 16. Schematic summary of the structure and strength of an atmospheric river based on dropsonde measurements analyzed in this study, and on corresponding reanalyses that provide the plan-view context. (a) Plan view including parent low pressure system, and associated cold, warm, stationary and warm-occluded surface fronts. IVT is shown by color fill (magnitude, kg m^{-1} s^{-1}) and direction in the core (white arrow). Vertically integrated water vapor (IWV, cm) is contoured. A representative length scale is shown. The position of the cross-section shown in panel (b) is denoted by the dashed line A-A'. (b) Vertical cross-section perspective, including the core of the water vapor transport in the atmospheric river (orange contours and color fill) and the pre-cold-frontal low-level jet (LLJ), in the context of the jet-front system and tropopause. Water vapor mixing ratio (green dotted lines, g kg^{-1}) and cross-section-normal isotachs (blue contours, m s^{-1}) are shown. Magnitudes of variables represent an average mid-latitude atmospheric river with lateral boundaries defined using the IVT threshold of 250 kg m^{-1} s^{-1}. Depth corresponds to the altitude below which 75% of IVT occurs. Adapted primarily from Ralph et al. 2004 and Cordeira et al. 2013.